Unified Lagrangian formulation for solid and fluid mechanics and FSI problems

*Alessandro Franci[1,2], Eugenio Oñate[1,2], Josep Maria Carbonell[1,2]
[1] International Center for Numerical Methods in Engineering (CIMNE)
Building C1, Campus North, UPC, Calle Gran Capitan s/n, 08034 Barcelona, Spain
[2] Universitat Politècnica de Catalunya (UPC), 08034 Barcelona, Spain

*falessandro@cimne.upc.edu

Abstract

We present a Lagrangian monolithic strategy for solving fluid-structure interaction (FSI) problems. The formulation is called Unified because fluids and solids are solved using the same solution scheme and unknown variables. The method is based on a mixed velocity-pressure formulation. Each time step increment is solved via an iterative partitioned two-step procedure. The Particle Finite Element Method (PFEM) is used for solving the fluid parts of the domain, while for the solid ones the Finite Element Method (FEM) is employed. Both velocity and pressure fields are interpolated using linear shape functions. For quasi-incompressible materials, the solution scheme is stabilized via the Finite Calculus (FIC) method. The stabilized elements for quasi-incompressible hypoelastic solids and Newtonian fluids are called VPS/S-element and VPS/F-element, respectively. Other two non-stabilized elements are derived for hypoelastic solids. One is based on a Velocity formulation (V-element) and the other on a mixed Velocity-Pressure scheme (VP-element). The algorithms for coupling the solid elements with the VPS/F fluid element are explained in detail. The Unified formulation is validated by solving benchmark FSI problems and by comparing the numerical solution to the ones published in the literature.

Keywords: Unified formulation, FSI, PFEM, Lagrangian formulation, quasi-incompressible materials

1. Introduction

The aim of this work is to derive a finite element formulation capable of solving the mechanics of a general continuum through a unique set of equations and unkown variables. The term 'general continuum' refers to a domain that may include compressible or quasi-incompressible solids and free surface fluids interacting together. For this reason, the formulation is termed *Unified*.

There are many reasons for undertaking the above objective. First of all, the Unified formulation allows us to solve fluids and solids by implementing and using a single solver. Furthermore, the unified solution scheme makes simpler the coupling for solving fluid-structure interaction (FSI) problems. This is because solids and fluids are analyzed as regions of the same continuum that differ only in the specific values of the material parameters. As a consequence, it is not required neither changing the variables, neither implementing the transfer of transmission conditions through the interface, as for other FSI algorithm. Additionally, the Unified formulation leads to a monolithic solution scheme for FSI problems. This gives the further advantages that the coupling is ensured strongly and an iteration loop is not required, differently from staggered procedures. Finally, the use of the same set of unknowns for the fluid and the solid domains improves the conditioning of the FSI solver, because the solution system does not include variables of different units of measure.

This formulation represents an extension of the coupling strategy for FSI problems presented by Idelsohn *et al.* [1]. The proposed Unified scheme allows us to couple a Velocity-Pressure Stabilized formulation for Fluids (VPS/F-element) with three different types of hypoelastic elements, namely the V, the VP and the VPS/S elements, corresponding to a Velocity, a Velocity-Pressure and a Velocity-Pressure Stabilized formulation, respectively. The governing equations are solved using an updated Lagrangian (UL) description. Each time step increment is solved via a two-step Gauss-Seidel partitioned iterative procedure. First, the momentum equations are solved for the velocity increments. Then, for the mixed elements, the continuity equation is solved for the pressure in the

updated configuration using the velocities computed at the first step.

The same linear interpolation is used for the velocity and the pressure fields. It is well known that, for incompressible (or quasi-incompressible) problems, this combination does not fulfill the $inf - sup$ condition [2] and a stabilization method is required. In this work the Finite Calculus (FIC) stabilization procedure [3, 4, 5, 6, 7, 8] is used. The FIC approach in mechanics is based on expressing the equations of balance of mass and momentum in a space-time domain of finite size. In addition to the standard terms of infinitesimal theory, the FIC form of the balance equations contains derivatives of the classical differential equations in mechanics multiplied by characteristic distances in space and time. In this work, the FIC stabilization procedure derived and validated in [9] for quasi-incompressible Newtonian fluids, has been used. In particular, the VPS/F-element has been implemented following precisely the scheme presented in [9].

Even though hypoelastic models are not free of drawbacks, above all when the elastic strains are large [10], hypoelasticity has been chosen for modeling the constitutive behavior of the solid elements presented in this work. This is because, thanks to its several analogies with the quasi-incompressible Newtonian model, hypoelasticity is the most adequate model for understanding the Unified formulation. However, the formulation does not preclude the use of other constitutive models, such as hyperelasticity, and neither the extension to hypoelasto-plasticity [11].

Introducing just small modifications, the same stabilization procedure is used also by the VPS/S-element for the analysis of quasi-incompressible hypoelastic solids. For solids far from the incompressible behavior, other two types of hypoelastic elements are presented, namely the V and the VP elements. The latter is based on the same scheme of the VPS/S-element, but the standard non-stabilized form is used for the continuity equation. Instead, the V-element is based on a pure velocity formulation. In this case, the stresses are computed using the velocity only and the continuity equation is not solved.

The V-element has the advantage that it has a reduced computational cost

with respect to the mixed elements because of the smaller number of degrees of freedom. Nevertheless, the VP-element guarantees a more accurate pressure field because the pressure is an unknown of the problem and it is not obtained from the velocity field after time integration and interpolation, as is should be done for the V-element. Furthermore, contrary to the V-element, the VP-element does not exhibit kinematic locking when materials with small compressibility are analyzed (however for incompressible or quasi incompressible materials the VPS-element must be used) [11].

The solid parts of the domain are solved using the Finite Element Method (FEM) [12], while for the VPS/F fluid element the Particle Finite Element Method (PFEM) [13] is used. The PFEM is a Lagrangian strategy that treats the mesh nodes of the domain as particles which can freely move and even separate from the rest of the fluid domain representing, for instance, the effect of water drops. A mesh connects the nodes discretizing the domain where the governing equations are solved using the FEM. The domain is continuously remeshed using a procedure that efficiently combines the Delaunay tesselation and the Alpha Shape Method [14]. These features make the PFEM the ideal numerical procedure to model and simulate free surface flows. In the last years, many scientific publications have shown the efficiency of the PFEM for solving free surface flow problems, [15, 16, 17]. The PFEM can be also used for other problems such as those involving thermal convection-diffusion [18, 19, 20], multi-fluids [21, 22], granular materials [23], bed erosion [24], FSI [25, 26], excavation [27] or industrial forming processes [28].

In the problems analyzed in this work, the solid undergoes large displacements but it does not suffer from extremely large distortions. In these cases, the remeshing of the solid is not necessary. In solids, in order to recover the elemental informations as the stresses or the plastic deformations, the remeshing must be associated to a transferring procedure from the elements of the old mesh to the ones of the new mesh. This operation represents an additional computational cost (that increases further the cost of the overall remeshing step) and it may introduce interpolation errors in the scheme. For this reason, it is

preferable to avoid the remeshing whenever it is not necessary. However, if the solid domains suffer from large distortions, the PFEM should be used also for the solid in order to avoid the distortion of the Lagrangian mesh (as done in [29]).

The FSI problem is solved with a monolithic scheme. This means that fluids and solids are solved within the same linear system of algebraic equations. Thanks to the many analogies in the analysis of fluids and solids, the implementation work for coupling the mechanics of fluids and solids is reduced to a proper assembly of the global linear system and to the geometric detection of the fluid-solid interface.

This text is organized as follows. In the next section, the governing equations of a general continuum are introduced. Then the constitutive laws used in this work for fluids and solids, namely the hypoelastic and quasi-incompressible Newtonian models, are presented. Section 4 is devoted to the linearization of the linear momentum equations. In the following section the continuity equation is discretized. In Section 6 the FIC-stabilized form of the continuity equation is given, first for Newtonian fluids and then for quasi-incompressible hypoelastic solids. The solution scheme of the Unified formulation for solving FSI problems is described for a generic time step in Section 7. The different expressions for the VPS/F-element for fluids and the V, VP, VPS/S elements for solids are detailed. The way to assemble the global linear system and to detect the fluid-solid interface is then explained. In Section 9 some numerical examples are given in order to validate the Unified formulation for FSI problems. Finally, the conclusions of this work are given.

2. Governing equations

The governing equations for a general continuum (either a fluid or a solid) are the linear momentum equations, with the corresponding boundary conditions, and the continuity equation. These equations are coupled with the constitutive relationships described in Section 3. In this work, the governing equations will

be written in the Updated Lagrangian (UL) formulation [30].

In order to avoid ambiguities, the variables and the matrices referred to fluids will be indentified by subindex 'f', and those refered to solids by subindex 's'. When both materials are involved, the subindex will be 's,f'.

For a general continuum, the local form of the linear momentum equations using the UL description reads [9]

$$\rho(\mathbf{X},t)\dot{\boldsymbol{v}}(\mathbf{X},t) - \frac{\partial \boldsymbol{\sigma}(\mathbf{X},t)}{\partial \mathbf{x}} - \boldsymbol{b}(\mathbf{X},t) = 0 \qquad in\ \Omega \times (0,T) \tag{1}$$

where ρ is the density of the material, $\dot{\boldsymbol{v}}$ is the time derivative of the velocities, $\boldsymbol{\sigma}$ is the Cauchy stress tensor and $\boldsymbol{b}$ is the body force vector. The variables within the brackets are the independent variables. In particular, $\mathbf{X}$ are the Lagrangian or material coordinates vector, $\mathbf{x}$ the Eulerian or spatial coordinates vector and t is the time. For simplicity, the independent variables will be not specified in the following.

The linear momentum equations are completed by the standard conditions at the Dirichlet (Γ_v) and Neumann (Γ_t) boundaries

$$v_i - v_i^p = 0 \qquad \text{on } \Gamma_v \tag{2}$$

$$\sigma_{ij} n_j - t_i^p = 0 \qquad \text{on } \Gamma_t \tag{3}$$

where v_i^p and t_i^p, $i = 1, ..., n_s$ are the prescribed velocities and the prescribed tractions, respectively.

The continuity equation is written in the form [31]

$$\frac{1}{\kappa_{f,s}} \dot{p} = d^v \tag{4}$$

where $\kappa_{f,s}$ is the bulk modulus for either the fluid or the solid, $\dot{p}$ is the time derivative of the pressure (defined positive in tension) and d^v is the volumetric strain rate which is defined as

$$d^v = d_{ii} \tag{5}$$

where $\boldsymbol{d}$ is the spatial strain rate tensor computed as a function of the velocities as

$$d_{ij} = \frac{1}{2}\left(\frac{\partial v_i}{\partial x_j} + \frac{\partial v_j}{\partial x_i}\right) \tag{6}$$

In the following, summation of terms for repeated indices is assumed, unless otherwise specified.

Note that, depending on the values of the material bulk modulus, the continuity equation in the form of Eq.(4) can be used for (standard) compressible, quasi-incompressible and fully incompressible materials, indifferently. For example, $\kappa = \infty$ yields $d^v = 0$ and canonical form of the continuity equation for incompressible materials is recovered.

For a general time interval $[{}^n t, {}^{n+1} t]$ Eq.(4) is discretized as

$$\frac{1}{\kappa_{f,s}} \frac{\Delta p}{\Delta t} = \frac{1}{\kappa_{f,s}} \frac{{}^{n+1}p - {}^{n}p}{\Delta t} = {}^{n+1}d^v \tag{7}$$

3. Constitutive laws

In this work, a hypoelastic constitutive law is used for solids, while for fluids the quasi-incompressible Newtonian model is considered. In the Unified formulation the constitutive relations for both fluids and solids are expressed in the following form

$$\boldsymbol{\sigma}^{\triangledown} = \boldsymbol{c}^{\triangledown\sigma} : \boldsymbol{d} \tag{8}$$

where $\boldsymbol{\sigma}^{\triangledown}$ is the Cauchy stress rate tensor, $\boldsymbol{c}^{\triangledown\sigma}$ is the fourth-order tangent moduli tensor and $\boldsymbol{d}$ is the deformation rate tensor.

In this section, the tangent moduli for the rate of the Cauchy stress $\boldsymbol{c}^{\triangledown\sigma}$ is given and the computation of the stresses is explained for both hypoelastic solids and Newtonian fluids.

3.1. Hypoelasticity

A hypoelastic body is defined by a direct relation between the rate of stress and the rate of strain [32]. In this work a Jaumann measure is used. It is well known that this model can lead to non-physical stress oscillations in simple shear problems with large deformations [33]. In these cases, a different hypoelastic measure should be used, as for example the Green-Naghdi one [34], [35]. However, for the rest of problems, including the ones selected in this work, the

Jaumann model can be freely used without experiencing the described shortcomings.

Considering a isotropic body and using a Jaumann measure of stress, the Cauchy stress rate tensor is computed as [36]

$$\boldsymbol{\sigma}^{\triangledown} = \boldsymbol{c}^{\sigma J} : \boldsymbol{d} \tag{9}$$

where the Jaumann fourth-order tangent moduli $\boldsymbol{c}^{\sigma J}$ is

$$c^{\sigma J}_{ijkl} = \kappa_s \delta_{ij}\delta_{kl} + \mu_s \left(\delta_{ik}\delta_{jl} + \delta_{il}\delta_{kj} - \frac{2}{3}\delta_{ij}\delta_{kl} \right) \quad , \quad \boldsymbol{c}^{\sigma J} = \kappa_s \boldsymbol{I} \otimes \boldsymbol{I} + 2\mu_s \mathbf{I}' \tag{10}$$

for a 2D problem, $\boldsymbol{c}^{\sigma J} = \begin{bmatrix} \kappa_s + \frac{4}{3}\mu_s & \kappa_s - \frac{2}{3}\mu_s & 0 \\ \kappa_s - \frac{2}{3}\mu_s & \kappa_s + \frac{4}{3}\mu_s & 0 \\ 0 & 0 & \mu_s \end{bmatrix}$

where κ_s is the solid bulk modulus computed from the Lamé parameters, λ_s and μ_s, as

$$\kappa_s = \lambda_s + \frac{2}{3}\mu_s, \tag{11}$$

$\boldsymbol{I}$ is the second-order identity tensor and $\mathbf{I}'$ is a fouth-order tensor computed as

$$\mathbf{I}' = \mathbf{I} - \frac{1}{3}\boldsymbol{I} \otimes \boldsymbol{I} \tag{12}$$

where $\mathbf{I}$ is the fouth-order symmetric identity tensor computed as $\mathrm{I}_{ijkl} = \frac{1}{2}\left(\delta_{ik}\delta_{jl} + \delta_{il}\delta_{kj}\right)$.

The material time derivative of the Cauchy stress rate is computed from the Jaumann measure of the Cauchy stress rate tensor as

$$\dot{\boldsymbol{\sigma}} = \boldsymbol{\sigma}^{\triangledown J} + \boldsymbol{\Omega} \tag{13}$$

where $\boldsymbol{\Omega}$ is a tensor that accounts for the rotations defined as

$$\boldsymbol{\Omega} = \boldsymbol{W} \cdot \boldsymbol{\sigma} + \boldsymbol{\sigma} \cdot \boldsymbol{W}^T \tag{14}$$

where $\boldsymbol{W}$ is the spin tensor

$$W_{ij} = \frac{1}{2}\left(\frac{\partial v_i}{\partial x_j} - \frac{\partial v_j}{\partial x_i} \right) \tag{15}$$

In this work, tensor $\boldsymbol{\Omega}$ is computed at the end of each time step.

Discretizing in time Eq.(13) for the time step interval $[{}^{n}t, {}^{n+1}t]$ and expanding the Cauchy stress rate, yields

$$\frac{{}^{n+1}\boldsymbol{\sigma} - {}^{n}\boldsymbol{\sigma}}{\Delta t} = \boldsymbol{c}^{\sigma J} : {}^{n+1}\boldsymbol{d} + {}^{n}\boldsymbol{\Omega} \tag{16}$$

In Eq.(16), ${}^{n}\boldsymbol{\Omega}$ can be viewed as a correction of the Cauchy stress tensor ${}^{n}\boldsymbol{\sigma}$. For this reason, the two tensors can be joined as

$${}^{n}\hat{\boldsymbol{\sigma}} = {}^{n}\boldsymbol{\sigma} + {}^{n}\boldsymbol{\Omega}\Delta t \tag{17}$$

Replacing Eq.(17) in (16), yields

$$\frac{{}^{n+1}\boldsymbol{\sigma} - {}^{n}\hat{\boldsymbol{\sigma}}}{\Delta t} = \boldsymbol{c}^{\sigma J} : {}^{n+1}\boldsymbol{d} \tag{18}$$

Note that, with the aim of reducing the non linearity of the problem, in Eq.(16) tensor $\boldsymbol{\Omega}$ is computed explicitely. Nevertheless, this is allowed only if the solid undergoes small rotations during a time step increment. Otherwise, $\boldsymbol{\Omega}$ should be computed implicitly and updated at each non linear iteration. However, note that in FSI problems the time step increment cannot be excessively large in order to avoid drawbacks as the excessive distortion of the fluid discretization or the penetration of fluid parts into the solid domain or through the rigid walls. For these reasons, generally the rotations of the solid within a time step are limited and the approximation of Eq.(16) can be accepted.
Substituting in Eq.(18) the expression for $\boldsymbol{c}^{\sigma J}$ using Eq.(10), yields

$$\frac{{}^{n+1}\boldsymbol{\sigma} - {}^{n}\hat{\boldsymbol{\sigma}}}{\Delta t} = \kappa_s \left(\boldsymbol{I} \otimes \boldsymbol{I}\right) : {}^{n+1}\boldsymbol{d} + 2\mu_s \mathbf{I}' : {}^{n+1}\boldsymbol{d} \tag{19}$$

The first and the second terms of the right hand side of Eq.(19) represent the increments in time of the pressure and the deviatoric part of the Cauchy stress tensor, respectively. Thus, for hypoelastic solids the time variation of the pressure can be computed in the same form as Eq.(7).

Thus, from Eqs.(19) and (7) one may compute the updated stresses using the velocities only or both the pressure and the velocities, as follows

$${}^{n+1}\boldsymbol{\sigma} = {}^{n}\hat{\boldsymbol{\sigma}} + \Delta t \left(\kappa_s \boldsymbol{I} \otimes \boldsymbol{I} + 2\mu_s \mathbf{I}'\right) : {}^{n+1}\boldsymbol{d} \tag{20}$$

$$^{n+1}\boldsymbol{\sigma} = {}^{n}\hat{\boldsymbol{\sigma}} + \Delta p\boldsymbol{I} + 2\Delta t\mu_s \mathbf{I}' : {}^{n+1}\boldsymbol{d} \tag{21}$$

Eqs.(20) and (21) will be used for computing the Cauchy stress tensor in the Velocity (V) and mixed Velocity-Pressure (VP) formulations, respectively.

3.2. Quasi-incompressible Newtonian fluids

The standard form of the constitutive relation for a Newtonian fluid reads

$$\boldsymbol{\sigma} = \boldsymbol{\sigma'} + p\boldsymbol{I} = 2\mu_f \boldsymbol{d}' + p\boldsymbol{I} \tag{22}$$

where μ_f is the fluid viscosity.

For a time interval $[n, n+1]$ Eq.(22) reads

$$^{n+1}\boldsymbol{\sigma} = 2\mu_f {}^{n+1}\boldsymbol{d}' + {}^{n+1}p\boldsymbol{I} \tag{23}$$

Quasi-incompressible fluids have a compressibility that is small enough to neglect the variations of density on time. However, unlike fully incompressible materials, they are not totally divergence-free and the volumetric strain rate is related to time change of the pressure via Eq.(7). Hence, for quasi-incompressible Newtonian fluids the pressure at ^{n+1}t can be computed as

$$^{n+1}p = {}^{n}p + \Delta t\kappa_f {}^{n+1}d^v \tag{24}$$

Subsituting Eq.(24) into (23) yields

$$^{n+1}\boldsymbol{\sigma} = (2\mu_f \mathbf{I}' + \Delta t\kappa_f \boldsymbol{I} \otimes \boldsymbol{I}) : {}^{n+1}\boldsymbol{d} + {}^{n}p\boldsymbol{I} \tag{25}$$

where $\mathbf{I}'$ is the fourth-order tensor defined in Eq.(12).

For convenience, Eq.(25) is rewritten as

$$\Delta\boldsymbol{\sigma} = {}^{n+1}\boldsymbol{\sigma} - {}^{n}\boldsymbol{\sigma} = \boldsymbol{c}^{\sigma}_{NF} : \boldsymbol{d} \tag{26}$$

where the following substitutions have been done

$$^{n}\boldsymbol{\sigma} = {}^{n}p\boldsymbol{I} \tag{27}$$

$$\boldsymbol{c}^{\sigma}_{NF} = 2\mu_f \mathbf{I}' + \Delta t\kappa_f \boldsymbol{I} \otimes \boldsymbol{I} \tag{28}$$

The aim of the Unified formulation is to reduce the differences in the analysis of fluids and solids. For this reason, the quasi-incompressible Newtonian constitutive law is written for the stress rate, similarly as for the hypoelastic model for solids. For Newtonian fluids, the rate of Cauchy stress can be simply computed with the material time derivative. Hence

$$\boldsymbol{\sigma}^{\nabla} = \dot{\boldsymbol{\sigma}} = \frac{\Delta \boldsymbol{\sigma}}{\Delta t} = \frac{\boldsymbol{c}_{NF}^{\sigma}}{\Delta t} : \boldsymbol{d} = \boldsymbol{c}_{NF}^{\nabla \sigma} : \boldsymbol{d} \tag{29}$$

where the tangent moduli tensor for the rate of the Cauchy stress $\boldsymbol{c}_{NF}^{\nabla \sigma}$ is

$$\boldsymbol{c}_{NF}^{\nabla \sigma} = \frac{2\mu_f}{\Delta t}\mathbf{I}' + \kappa_f \boldsymbol{I} \otimes \boldsymbol{I} \tag{30}$$

Note that Eq.(29) has the same structure as Eq.(8).

$$\text{For a 2D problem, } \boldsymbol{c}_{NF}^{\nabla \sigma} = \begin{bmatrix} \kappa_f + \frac{4}{3\Delta t}\mu_f & \kappa_f - \frac{2}{3\Delta t}\mu_f & 0 \\ \kappa_f - \frac{2}{3\Delta t}\mu_f & \kappa_f + \frac{4}{3\Delta t}\mu_f & 0 \\ 0 & 0 & \frac{\mu_f}{\Delta t} \end{bmatrix}$$

4. Linearization of the momentum equations

In the UL description used in this work, the governing equations are integrated over the unknown configuration Ω (the so-called updated configuration) and the space derivatives are computed with respect to the spatial coordinates.

From Eq.(1), integrating over Ω and after standard transformations, the Galerkin approximation of the Principle of Virtual Power for a node I is obtained as [36]

$$\underbrace{\int_{\Omega} N_I \rho d\Omega \; \dot{v}_i}_{f_{Ii}^{dyn}} + \underbrace{\int_{\Omega} \frac{\partial N_I}{\partial x_j}\sigma_{ij} d\Omega}_{f_{Ii}^{int}} = \underbrace{\int_{\Omega} N_I b_i d\Omega + \int_{\Gamma_t} N_I t_i^p d\Gamma}_{f_{Ii}^{ext}} \tag{31}$$

where N_I is the linear shape function for node I and $\boldsymbol{f}^{dyn}$, $\boldsymbol{f}^{int}$ and $\boldsymbol{f}^{ext}$ are the dynamic, internal and external force vectors, respectively, expressed in the UL framework.

For this work we use linear 3-noded triangles (for 2D problems) and 4-noded tetrahedra (for 3D problems) to interpolate the velocity and pressure variables, as appropriate.

For convenience, the linearization of the internal forces $\boldsymbol{f}^{int}$ is performed in the known configuration Ω_0, as for a total Lagrangian (TL) description. This is because in the UL form also the spatial derivative and the integration domain depend on the deformation, and hence on the time, and this complicates the linearization. For this reason, the UL linearized form will be obtained later by applying a push-forward transformations on the TL form. Instead, the linearization of the dynamics forces $\boldsymbol{f}^{dyn}$ will be performed directly in the updated configuration.

4.1. Internal components of the tangent matrix

Applying a standard pull back tranformation to $\boldsymbol{f}^{int}$ from the unknown domain Ω to the known one Ω_0 [36], the internal forces for a TL description ${}^{TL}\boldsymbol{f}^{int}$ read

$$ {}^{TL}f_{Ii}^{int} = \int_{\Omega_0} \frac{\partial N_I}{\partial X_j} P_{ij} d\Omega_0 \tag{32} $$

where $\boldsymbol{P}$ is the first Piola-Kirchhoff stress tensor. All the variables with vectors subscript $(\cdot)_0$ refer to the last known configuration. For the sake of clarity, the terms referred to the TL description are denoted with the left upper index ${}^{TL}(\cdot)$. Unless otherwise specified, the variables belong to the UL description.

In the proposed Unified formulation, the constitutive relations for both fluids and solids are expressed in rate form. Hence it is more convenient to perform the linearization of the material derivative of the internal forces and then integrate for the time step increment Δt. The material time derivative of Eq.(32) is

$$ {}^{TL}\dot{f}_{Ii}^{int} = \int_{\Omega_0} \frac{\partial N_I}{\partial X_j} \dot{P}_{ij} d\Omega_0 \tag{33} $$

The first Piola-Kirchhoff stress tensor $\boldsymbol{P}$ is not typically used because it is not symmetric and its rate is a non-objective measure. For these reasons, in the TL framework it is more convenient to work with the second Piola-Kirchhoff stress

tensor $\boldsymbol{S}$ and its rate. These stress rate measures are related each other via the following relation

$$\dot{P}_{ij} = \dot{S}_{ir} F^T_{rj} + S_{ir} \dot{F}^T_{rj} \tag{34}$$

where $\boldsymbol{F}$ is the deformation gradient tensor defined as

$$F_{ij} = \frac{\partial x_i}{\partial X_j} \tag{35}$$

Substituting Eq.(34) into (33), and analyzing an infinitesimal increment yields

$$^{TL}\delta \dot{f}^{int}_{Ii} = \underbrace{\int_{\Omega_0} \frac{\partial N_I}{\partial X_j} F_{ir} \delta \dot{S}_{jr} d\Omega_0}_{^{TL}\delta \dot{f}^{m}_{Ii}} + \underbrace{\int_{\Omega_0} \frac{\partial N_I}{\partial X_j} S_{ir} \delta \dot{F}^T_{rj} d\Omega_0}_{^{TL}\delta \dot{f}^{g}_{Ii}} \tag{36}$$

In Eq.(36) the increment of the material time derivative of the internal forces has been split into the material and the geometric parts, $^{TL}\delta \dot{\boldsymbol{f}}^m$ and $^{TL}\delta \dot{\boldsymbol{f}}^g$, respectively. The former accounts for the material response through the rate of the second Piola-Kirchhoff stress tensor. The second term is the initial stress term that contains the information of the updated stress field.

4.1.1. Material tangent matrix

The rate of the second Piola-Kirchhoff stress tensor $\boldsymbol{S}$ is related to the deformation rate through the tangent constitutive tensor as

$$\dot{S}_{ij} = C_{ijkl} \dot{E}_{kl} \tag{37}$$

where $\boldsymbol{C}$ is a fourth-order tensor and $\dot{\boldsymbol{E}}$ is the rate of the Green-Lagrange strain tensor.

Substituting Eq.(37) into the term $^{TL}\delta \dot{\boldsymbol{f}}^m$ of Eq.(36), yields

$$^{TL}\delta \dot{f}^{m}_{Ii} = \int_{\Omega_0} \frac{\partial N_I}{\partial X_j} F_{ir} C_{jrkl} \delta \dot{E}_{kl} d\Omega_0 \tag{38}$$

The rate of the Green-Lagrange strain tensor can be expressed in terms of the nodal velocities as

$$\dot{E}_{kl} = \frac{\partial N_J}{\partial X_l} F_{sk} \bar{v}_{Js} \tag{39}$$

In Eq.(39) and in the following, $\bar{(\cdot)}$ denotes a nodal value (*e.g.* $\bar{v}_{Js}$ is the s-component of the velocity of node J).

Substituting Eq.(39) in (38), yields

$$ {}^{TL}\delta\dot{f}^m_{Ii} = \int_{\Omega_0} \frac{\partial N_I}{\partial X_j} F_{ir} C_{jrkl} \frac{\partial N_J}{\partial X_l} F_{sk} d\Omega_0 \; \delta\bar{v}_{Js} \tag{40} $$

In order to obtain the increment of the internal forces, the material time derivative of the internal forces increment is integrated over a time step increment Δt as

$$ {}^{TL}\delta\boldsymbol{f}^m = {}^{TL}\delta\dot{\boldsymbol{f}}^m \Delta t \tag{41} $$

From Eqs.(40) and (41), yields

$$ {}^{TL}\delta f^m_{Ii} = \int_{\Omega_0} \frac{\partial N_I}{\partial X_j} F_{ir} \Delta t C_{jrkl} \frac{\partial N_J}{\partial X_l} F_{sk} d\Omega_0 \; \delta\bar{v}_{Js} \tag{42} $$

The material tangent matrix for the UL framework is obtained by applying a push-forward transformation on each term of Eq.(42) and integrating over the updated domain Ω. The following relations hold

$$ d\Omega_0 = \frac{d\Omega}{J} \tag{43} $$

$$ \frac{\partial N_I}{\partial X_j} = \frac{\partial N_I}{\partial x_k} F_{kj} \tag{44} $$

$$ C^{\nabla\sigma}_{ijkl} = F^{-1}_{mi} F^{-1}_{nj} F^{-1}_{ok} F^{-1}_{pl} c^{\nabla\sigma}_{mnop} J \tag{45} $$

where $\boldsymbol{c}^{\nabla\sigma}$ is the tangent moduli for the rate of the Cauchy stress $\boldsymbol{\sigma}^{\nabla}$.

Substituting Eqs.(43-45) into (42) and using the minor symmetries, yields

$$ \delta f^m_{Ir} = \int_{\Omega} \frac{\partial N_I}{\partial x_k} \delta_{ri} \Delta t \; c^{\nabla\sigma}_{kijl} \frac{\partial N_J}{\partial x_l} \delta_{sj} d\Omega \; \delta\bar{v}_{Js} \tag{46} $$

Therefore, the expressions of the material tangent matrix for the velocity increments in UL framework in the indicial and Voigt notation read, respectively

$$ K^m_{IJrs} = \int_{\Omega} \frac{\partial N_I}{\partial x_k} \delta_{ri} \Delta t \; c^{\nabla\sigma}_{kijl} \frac{\partial N_J}{\partial x_l} \delta_{sj} d\Omega \;, \;\; \boldsymbol{K}^m_{IJ} = \int_{\Omega^e} \boldsymbol{B}^T_I \Delta t \left[\boldsymbol{c}^{\nabla\sigma}\right] \boldsymbol{B}_J d\Omega \tag{47} $$

For the node I of a 2D element, matrix $\boldsymbol{B}$ is

$$ \mathbf{B}_I = \begin{bmatrix} \dfrac{\partial N_I}{\partial x} & 0 & \dfrac{\partial N_I}{\partial y} \\ 0 & \dfrac{\partial N_I}{\partial y} & \dfrac{\partial N_I}{\partial x} \end{bmatrix}^T \tag{48} $$

4.1.2. Geometric tangent matrix

The geometric tangent matrix in the UL framework is derived using the same procedure as for the material component.

From Eq.(36)

$$^{TL}\delta \dot{f}^g_{Ii} = \int_{\Omega_0} \frac{\partial N_I}{\partial X_j} S_{ir} \delta \dot{F}^T_{rj} d\Omega_0 \tag{49}$$

where the rate of the deformation gradient $\dot{\boldsymbol{F}}$ is defined as

$$\dot{F}_{ij} = \frac{\partial N_J}{\partial X_i} \bar{v}_{Jj} \tag{50}$$

Substituting Eq.(50) into Eq.(49), the geometric components of the internal power in the TL description can be written as

$$^{TL}\delta \dot{f}^g_{Ii} = \int_{\Omega_0} \frac{\partial N_I}{\partial X_j} S_{ir} \frac{\partial N_J}{\partial X_r} d\Omega_0 \ \delta \bar{v}_{Jj} \tag{51}$$

Integrating Eq.(51) in time for a time step increment Δt yields

$$^{TL}\delta f^g_{Ii} = \int_{\Omega_0} \frac{\partial N_I}{\partial X_j} \Delta t S_{ir} \frac{\partial N_J}{\partial X_r} d\Omega \ \delta \bar{v}_{Jj} \tag{52}$$

In order to recover the UL form, the Piola identity has to be recalled, *i.e.*

$$\boldsymbol{S} = \boldsymbol{F}^{-1} \boldsymbol{\sigma} \boldsymbol{F}^{-T} J \tag{53}$$

Substituting Eqs.(43), (44) and (53) into (52) and using the symmetries, yields

$$\delta f^g_{Ir} = \int_{\Omega} \frac{\partial N_I}{\partial x_j} \Delta t \sigma_{jk} \frac{\partial N_J}{\partial x_k} d\Omega \delta_{rs} \delta \bar{v}_{Js} \tag{54}$$

The geometric part of the tangent matrix for the increments of velocity is obtained from Eq.(54) as

$$K^g_{IJrs} = \int_{\Omega} \frac{\partial N_I}{\partial x_j} \Delta t \sigma_{jk} \frac{\partial N_J}{\partial x_k} d\Omega \delta_{rs} \ , \ \boldsymbol{K}^g_{IJ} = \boldsymbol{I} \int_{\Omega} \boldsymbol{\beta}^T_I \Delta t \boldsymbol{\sigma} \boldsymbol{\beta}_J d\Omega \tag{55}$$

where for 2D problems $\boldsymbol{\beta}_I = \begin{bmatrix} \dfrac{\partial N_I}{\partial x} & \dfrac{\partial N_I}{\partial y} \end{bmatrix}^T$.

4.2. Dynamic component of the tangent matrix

In this work, the implicit Newmark's integration rule has been adopted. In particular, the Newmark's parameters chosen are $\beta = \frac{1}{4}$ and $\gamma = \frac{1}{2}$ [36]. Ac-

cording to this unconditionally stable scheme, the accelerations $\dot{\boldsymbol{v}}$ and the displacements $\boldsymbol{u}$ are computed, respectively, as

$$^{n+1}\dot{\boldsymbol{v}} = \frac{2}{\Delta t}\left(^{n+1}\boldsymbol{v} - {}^{n}\boldsymbol{v}\right) - {}^{n}\dot{\boldsymbol{v}} \tag{56}$$

$$^{n+1}\boldsymbol{u} = {}^{n}\boldsymbol{u} + \frac{\Delta t}{2}\left(^{n+1}\boldsymbol{v} + {}^{n}\boldsymbol{v}\right) \tag{57}$$

Replacing Eq.(56) into the dynamic term f_{Ii}^{dyn} of Eq.(31), and differentiating with respect to velocity increments, the dynamic component of the tangent matrix (also known as the mass matrix) is obtained as

$$K_{IJij}^{\rho} = \delta_{ij}\int_{\Omega} N_I \frac{2\rho}{\Delta t} N_J d\Omega \ , \ \boldsymbol{K}_{IJ}^{\rho} = \boldsymbol{I}\int_{\Omega} N_I \frac{2\rho}{\Delta t} N_J d\Omega \tag{58}$$

4.3. Incremental solution scheme

The linear momentum equations are solved iteratively for the velocity increments. For each iteration i the following linear system is solved

$$\boldsymbol{K}^i \boldsymbol{\Delta}\bar{\boldsymbol{v}} = \boldsymbol{R}^i \tag{59}$$

with

$$\boldsymbol{K}^i = \boldsymbol{K}^m(^{n+1}\bar{\boldsymbol{x}}^i, \boldsymbol{c}^{\triangledown\sigma}) + \boldsymbol{K}^g(^{n+1}\bar{\boldsymbol{x}}^i, \boldsymbol{\sigma}^i) + \boldsymbol{K}^{\rho}(^{n+1}\bar{\boldsymbol{x}}^i) \tag{60}$$

where $\boldsymbol{K}_{IJ}^m$, $\boldsymbol{K}_{IJ}^g$ and $\boldsymbol{K}_{IJ}^{\rho}$ are respectively given in Eq.(47), Eq.(55) and Eq.(58), and

$$R_{Ii}^i = \int_{\Omega} N_I \rho N_J d\Omega \ \bar{v}_{Ji}^i + \int_{\Omega} \frac{\partial N_I}{\partial x_j}\sigma_{ij}^i d\Omega - \int_{\Omega} N_I {}^{n+1}b_i d\Omega - \int_{\Gamma_t} N_I {}^{n+1}t_i^p d\Gamma \tag{61}$$

The fourth-order constitutive tangent moduli tensor $\boldsymbol{c}^{\triangledown\sigma}$ of matrix $\boldsymbol{K}^m$ (Eq.(47)) is $\boldsymbol{c}_{NF}^{\triangledown\sigma}$ (Eq.(30)) for a Newtonian fluid while for a hypoelastic solid is $\boldsymbol{c}^{\sigma J}$ (Eq.(10)).

In the analysis of quasi-incompressible Newtonian fluids, the volumetric part of the material component of the tangent matrix $\boldsymbol{K}^m$ can compromise the conditioning of the linear system [37, 38, 39]. In order to prevent the numerical instabilities originated by the ill-conditioning of the tangent matrix, the actual bulk modulus of the fluid κ_f is replaced by a reduced pseudo bulk modulus κ_p,

defined as a $\kappa_p = \theta\kappa_f$. The pseudo bulk modulus is predicted *a priori* using the strategy described in [40]. In the mentioned publication it has been shown that using the pseudo bulk modulus in the tangent matrix of the linear momentum equations (in the continuity equation the actual bulk modulus is used) is extremely helpful for improving the conditioning of the problem and it does not alter the numerical results.

For Newtonian fluids the stress tensor $\boldsymbol{\sigma}$ is computed via Eq.(25). For hypoelastic solids, if a velocity formulation is used the stresses are computed via Eq.(20). In the context of a mixed velocity-pressure formulation, the Cauchy stress tensor $\boldsymbol{\sigma}$ is computed with Eq.(21).

5. Discretized form of the mass balance equation

For the solid VP-element the continuity equation is solved in the standard non-stabilized form of Eq.(4). The Galerkin approximation of Eq.(4) for the same linear shape functions $\boldsymbol{N}$ used for the velocity is

$$\int_\Omega N_I \frac{1}{\kappa_s} N_J d\Omega \dot{\bar{p}_J} - \int_\Omega N_I \frac{\partial N_J}{\partial x_i} d\Omega \bar{v}_{iJ} = 0 \tag{62}$$

Regarding the time integration, a first order scheme has been adopted for the pressure. Thus, for a time interval $[{}^n t, {}^{n+1} t]$ of duration Δt the first and the second variations in time of the pressure are computed as

$${}^{n+1}\dot{\boldsymbol{p}} = \frac{{}^{n+1}\boldsymbol{p} - {}^{n}\boldsymbol{p}}{\Delta t} \tag{63}$$

$${}^{n+1}\ddot{\boldsymbol{p}} = \frac{{}^{n+1}\boldsymbol{p} - {}^{n}\boldsymbol{p}}{\Delta t^2} - \frac{{}^{n}\dot{\boldsymbol{p}}}{\Delta t} \tag{64}$$

Introducing Eq.(63) in (62), the discretized form of the continuity equation solved for the pressure is

$$\frac{1}{\Delta t}\boldsymbol{M}_1 {}^{n+1}\bar{\boldsymbol{p}} = \frac{1}{\Delta t}\boldsymbol{M}_1 {}^{n}\bar{\boldsymbol{p}} + \boldsymbol{Q}^{T\,n+1}\bar{\boldsymbol{v}} \tag{65}$$

where the matrices introduced in Eq.(65) are defined in Box 1.

$$M_{1_{IJ}} = \int_{\Omega^e} N_I \frac{1}{\kappa_s} N_J d\Omega \ , \ \mathbf{Q}_{IJ} = \int_{\Omega^e} \mathbf{B}_I^T \mathbf{m} N_J d\Omega \ \text{ with } \ \mathbf{m} = [1,1,0]^T$$

Box 1. Matrices and vectors of the continuity equation (Eq.(65)) for the VP-element.

6. Stabilized FIC form of the mass balance equation

In order to deal with quasi and fully incompressible materials the numerical scheme needs to be stabilized. This is because the interpolation orders of the velocity and pressure fields do not fullfil the so-called *LBB inf − sup condition* [2]. The required stabilization is introduced for both the VPS/F and the VPS/S elements via the Finite Calculus (FIC) technique presented in [9]. In the mentioned work, a FIC stabilized finite element formulation for quasi-incompressible Newtonian fluids is derived and validated for several free surface flow problems, highlighting its excellent mass preservation features. The derivation of the stabilization technique lies outside the objectives of this work and the details can be found in [9]. Basically, the linear momentum equations do not change and are counted, with both the second order FIC form in space and the first order FIC form in time of the quasi-incompressible mass balance equation [7, 8], for deriving the stabilized form of the mass balance equation in a consistent manner.

For the VPS/F-element the same FIC form of the mass balance equation derived in [9] can be used because both refer to Newtonian fluids. Hence, for the VPS/F-element, the FIC-stabilized form of the mass balance equation, after FEM discretization, reads

$$\int_\Omega \frac{1}{\kappa_f} \mathbf{N}^T \mathbf{N} \frac{D\bar{\boldsymbol{p}}}{Dt} d\Omega + \int_\Omega \frac{\tau_f \rho}{\kappa_f} \mathbf{N}^T \mathbf{N} \frac{D^2 \bar{\boldsymbol{p}}}{Dt^2} d\Omega - \int_\Omega \mathbf{N}^T \mathbf{m}^T \mathbf{B} \bar{\boldsymbol{v}} d\Omega + \\ + \int_\Omega \tau_f (\boldsymbol{\nabla} \mathbf{N})^T \boldsymbol{\nabla} \mathbf{N} \bar{\boldsymbol{p}} d\Omega + \int_{\Gamma_t} \frac{2\tau_f}{h_n} \mathbf{N}^T \mathbf{N} \bar{\boldsymbol{p}} d\Gamma - \boldsymbol{f}_p = 0 \qquad (66)$$

where for triangular elements

$$\boldsymbol{\nabla}\mathbf{N}^T = \begin{bmatrix} \boldsymbol{\nabla}N_1 \\ \boldsymbol{\nabla}N_2 \\ \boldsymbol{\nabla}N_3 \end{bmatrix} \text{ with } \boldsymbol{\nabla} = \begin{Bmatrix} \dfrac{\partial}{\partial x} \\ \dfrac{\partial}{\partial y} \end{Bmatrix} \text{ and } \mathbf{N} = [\mathbf{N}_1, \mathbf{N}_2, \mathbf{N}_3]^T \tag{67}$$

and τ is the stabilization parameter given by

$$\tau_f = \left(\frac{8\mu_f}{h^2} + \frac{2\rho}{\delta} \right)^{-1} \tag{68}$$

where h and δ are characteristic distances in space and time, respectively. In practice, h and δ have the same order of magnitude of the element size and the time step increment, respectively. Details of the derivation of Eq.(66) can be found in [9].

In order to use the same form of Eq.(66) [9] for quasi-incompressible hypoelastic solids as for the VPS/F-element, the fluid parameters (the viscosity μ_f and the bulk modulus κ_f) are replaced by the equivalent parameters for the solid. The similarity between the constitutive expression for Newtonian fluids and hypoelastic solids is evident comparing expression used for computing the Cauchy stress tensor increment for both cases.

For quasi-incompressible Newtonian fluids Eq.(26) holds and, for clarity purposes, here is rewritten as

$$\Delta\boldsymbol{\sigma}_f = 2\mu_f \mathbf{I}' : \boldsymbol{d} + \Delta t \kappa_f \boldsymbol{I} \otimes \boldsymbol{I} : \boldsymbol{d} \tag{69}$$

From Eqs.(19), the increment of the Cauchy stress for hypoelastic solids is

$$\Delta\boldsymbol{\sigma}_s = 2\Delta t \mu_s \mathbf{I}' : \boldsymbol{d} + \Delta t \kappa_s \boldsymbol{I} \otimes \boldsymbol{I} : \boldsymbol{d} \tag{70}$$

Eqs.(69) and (70) show the duality between quasi-incompressible Newtonian and hypoelastic constitutive laws. In the former the deviatoric and the volumetric parts of the Cauchy stress tensor are controled by the dynamic viscosity μ_f and the bulk modulus κ_f, respectively. The equivalent roles in hypoelastic solids are taken by the second Lamè parameter scaled by the time increment ($\Delta t \mu_s$) and the bulk modulus κ_s.

Thanks to this equivalence, the FIC-based stabilized mass continuity equation for the VPS/S hypoelastic element can be written (after FEM discretization) as

$$\int_\Omega \frac{1}{\kappa_s}\mathbf{N}^T\mathbf{N}\frac{D\bar{\boldsymbol{p}}}{Dt}d\Omega + \int_\Omega \frac{\tau_s\rho}{\kappa_s}\mathbf{N}^T\mathbf{N}\frac{D^2\bar{\boldsymbol{p}}}{Dt^2}d\Omega - \int_\Omega \mathbf{N}^T\mathbf{m}^T\mathbf{B}\bar{\boldsymbol{v}}d\Omega + \\ + \int_\Omega \tau_s(\boldsymbol{\nabla}\mathbf{N})^T\boldsymbol{\nabla}\mathbf{N}\bar{\boldsymbol{p}}d\Omega + \int_{\Gamma_t}\frac{2\tau_s}{h_n}\mathbf{N}^T\mathbf{N}\bar{\boldsymbol{p}}d\Gamma - \boldsymbol{f}_p = 0 \tag{71}$$

where τ_s is the stabilization parameter given by

$$\tau_s = \left(\frac{8\Delta t\mu_s}{h^2} + \frac{2\rho}{\delta}\right)^{-1} \tag{72}$$

We highlight again the analogy between the discretized (stabilized) FIC-form of the mass balance equation for fluids (Eq.(66)) and solids (Eq.71).

Eqs.(66) and (71) can be written in an unified matrix form for both fluids and solids as

$$\mathbf{M}_{1(f,s)}\dot{\bar{\boldsymbol{p}}} + \mathbf{M}_{2(f,s)}\ddot{\bar{\boldsymbol{p}}} - \mathbf{Q}^T\bar{\boldsymbol{v}} + (\mathbf{L}_{(f,s)} + \mathbf{M}_{b(f,s)})\bar{\boldsymbol{p}} - \boldsymbol{f}_{p(f,s)} = \mathbf{0} \tag{73}$$

The matrices and vectors in Eq.(73) for Newtonian fluids (VPS/F-element) and hypoelastic solids (VPS/S-element) are given in Box 2 and 3, respectively.

$$M_{1f_{IJ}} = \int_\Omega \frac{1}{\kappa_f}N_IN_Jd\Omega \ , \ M_{2f_{IJ}} = \int_\Omega \tau_f\frac{\rho}{\kappa_f}N_IN_Jd\Omega$$
$$M_{bf_{IJ}} = \int_{\Gamma_t}\frac{2\tau_f}{h_n}N_IN_Jd\Gamma \ , \ L_{f_{IJ}} = \int_\Omega \tau_f(\boldsymbol{\nabla}^TN_I)\boldsymbol{\nabla}N_Jd\Omega$$
$$f_{pf_I} = \int_{\Gamma_t}\tau_fN_I\left[\rho\frac{Dv_n}{Dt} - \frac{2}{h_n}(2\mu_fd_n - t_n)\right]d\Gamma - \int_{\Omega^e}\tau_f\boldsymbol{\nabla}^TN_I\boldsymbol{b}d\Omega$$

Box 2. Matrices and vectors of Eq.(73) for the VPS/F-element.

Introducing the time integration of the pressure (Eqs.(63) and (64)) into Eq.(73) and solving the stabilized continuity equation for the nodal pressures, yields

$$\boldsymbol{H}_{f,s}\bar{\boldsymbol{p}}^{i+1} = \boldsymbol{F}_{p(f,s)}(\bar{\boldsymbol{v}},\bar{\boldsymbol{p}}) \tag{74}$$

where

$$\boldsymbol{H}_{f,s} = \left(\frac{1}{\Delta t}\mathbf{M}_{1(f,s)} + \frac{1}{\Delta t^2}\mathbf{M}_{2(f,s)} + \mathbf{L}_{f,s} + \mathbf{M}_{b(f,s)}\right) \tag{75}$$

$$
\begin{aligned}
&M_{1s_{IJ}} = \int_\Omega \frac{1}{\kappa_s} N_I N_J d\Omega \ , \ M_{2s_{IJ}} = \int_\Omega \tau_s \frac{\rho}{\kappa_s} N_I N_J d\Omega \\
&M_{bs_{IJ}} = \int_{\Gamma_t} \frac{2\tau_s}{h_n} N_I N_J d\Gamma \ , \ L_{s_{IJ}} = \int_\Omega \tau_s (\boldsymbol{\nabla}^T N_I) \boldsymbol{\nabla} N_J d\Omega \\
&f_{ps_I} = \int_{\Gamma_t} \tau_s N_I \left[\rho \frac{Dv_n}{Dt} - \frac{2}{h_n} (2\Delta t \mu_s d_n - t_n) \right] d\Gamma - \int_{\Omega^e} \tau_s \boldsymbol{\nabla}^T N_I \boldsymbol{b} d\Omega
\end{aligned}
$$

Box 3. Matrices and vectors of Eq.(73) for the VPS/S-element.

and

$$
\boldsymbol{F}_{p(f,s)} = \frac{\mathbf{M}_{1(f,s)}}{\Delta t} {}^n\bar{\boldsymbol{p}} + \frac{\mathbf{M}_{2(f,s)}}{\Delta t^2} \left({}^n\bar{\boldsymbol{p}} + {}^n\dot{\bar{\boldsymbol{p}}} \Delta t \right) + \mathbf{Q}^T \ \bar{\boldsymbol{v}} + \boldsymbol{f}_{p(f,s)} \tag{76}
$$

7. Solution scheme

Each time step is solved using a two-step Gauss-Seidel iterative procedure. First the linear momentum equations are solved for the velocity increments according to Eq.(59). Then the continuity equation is solved for the pressure in the updated configuration. For the VPS/F-element the stabilized form of Eq.(74) is solved using the matrices of Box 1. For quasi-incompressible solids, the VPS/S-element is used, hence the continuity equation is solved using the stabilized form of Eq.(74) and the matrices given in Box 2. Instead, for solids far from the incompressible limit, both the V and the VP elements can be used. With the VP-element, the non-stabilized form of the continuity equation (Eq.(65)) is solved. On the contrary, if the V-element is used the continuity equation is not computed. In Table 1, the essential features of each one of the elements presented in this work are summarized.

Concerning the degrees of freedom, each node of the mesh is characterized by a single set of kinematic variables. This means that the degrees of freedom for the solid and fluid velocities coincide also at the interface nodes. On the contrary, in order to guarantee the correct boundary conditions for the stresses, each interface node has a degree of freedom for the pressure of the fluid and another one for the pressure of the solid. This requires solving twice the continuity equation at the fluid-solid interface: once for the VPS/F-element and

	Element			
	V	**VP**	**VPS/S**	**VPS/F**
Constitutive law	Hypoelastic solid	Hypoelastic solid	Hypoelastic solid	Newtonian fluid
Momentum equations	Eq.(59)	Eq.(59)	Eq.(59)	Eq.(59)
$\boldsymbol{c}^{\nabla\sigma}$	$\boldsymbol{c}^{\sigma J}$, Eq.(10)	$\boldsymbol{c}^{\sigma J}$, Eq.(10)	$\boldsymbol{c}^{\sigma J}$, Eq.(10)	$\boldsymbol{c}_{NF}^{\nabla\sigma}$, Eq.(30)
$\boldsymbol{\sigma}$	Eq.(20)	Eq.(21)	Eq.(21)	Eq.(23)
Continuity equation	-	Eq.(65) Box 1	Eq.(74) Box 3	Eq.(74) Box 2

Table 1: Essential features of the V, VP, VPS/S and VPS/F elements.

once for the VP or the VPS/S solid elements.

For the sake of clarity, the coupling algorithms for the V-element and the mixed elements (the VP and VPS/S elements) are presented separately.

For a generic time interval $[{}^{n}t, {}^{n+1}t]$, Algorithm 1 describes all the steps required for solving the FSI problem using the VPS/F-element for fluids and the V-element for solids.

For each iteration i:

1. Compute the nodal velocity increments $\boldsymbol{\Delta\bar{v}}_{s,f}$:

$\boldsymbol{K}^i_{s,f}\boldsymbol{\Delta\bar{v}}_{s,f} = \boldsymbol{R}^i_{s,f}(\bar{\boldsymbol{v}}^i_{s,f}, \bar{\boldsymbol{p}}^i_f)$

where for fluids $\boldsymbol{K}^i_f = \boldsymbol{K}^m(\bar{\boldsymbol{x}}^i, \boldsymbol{c}^{\triangledown\sigma}_{NF}) + \boldsymbol{K}^g(\bar{\boldsymbol{x}}^i, \boldsymbol{\sigma}^i_f) + \boldsymbol{K}^\rho(\bar{\boldsymbol{x}}^i)$

and for solids $\boldsymbol{K}^i_s = \boldsymbol{K}^m(\bar{\boldsymbol{x}}^i, \boldsymbol{c}^{\sigma J}) + \boldsymbol{K}^g(\bar{\boldsymbol{x}}^i, \boldsymbol{\sigma}^i_s) + \boldsymbol{K}^\rho(\bar{\boldsymbol{x}}^i)$

2. Update the nodal velocities: ${}^{n+1}\bar{\boldsymbol{v}}^{i+1}_{s,f} = {}^{n+1}\bar{\boldsymbol{v}}^i_{s,f} + \boldsymbol{\Delta\bar{v}}_{s,f}$

3. Update the nodal coordinates: ${}^{n+1}\bar{\boldsymbol{x}}^{i+1}_{s,f} = {}^{n+1}\bar{\boldsymbol{x}}^i_{s,f} + \bar{\boldsymbol{u}}_{s,f}(\boldsymbol{\Delta\bar{v}}_{s,f})$

4. Compute the fluid nodal pressures $\bar{\boldsymbol{p}}^{i+1}_f$: $\boldsymbol{H}_f\bar{\boldsymbol{p}}^{i+1}_f = \boldsymbol{F}_{pf}(\bar{\boldsymbol{v}}^{i+1}_f, \bar{\boldsymbol{p}}^i_f)$

where $\boldsymbol{H}_f = \left(\frac{1}{\Delta t}\mathbf{M}_{1f} + \frac{1}{\Delta t^2}\mathbf{M}_{2f} + \mathbf{L}_f + \mathbf{M}_{bf}\right)$

and $\boldsymbol{F}_{pf} = \frac{\mathbf{M}_{1f}}{\Delta t}{}^n\bar{\boldsymbol{p}}_f + \frac{\mathbf{M}_{2f}}{\Delta t^2}\left({}^n\bar{\boldsymbol{p}}_f + {}^n\dot{\bar{\boldsymbol{p}}}_f\Delta t\right) + \mathbf{Q}^T\ \bar{\boldsymbol{v}}^{i+1}_f + \boldsymbol{f}_{pf}$

5. Compute the updated stress measures

for fluids: $\boldsymbol{\sigma}^{i+1}_f = 2\mu\boldsymbol{d}'_f(\bar{\boldsymbol{v}}^{i+1}_f) + p^{i+1}_f\boldsymbol{I}$

for solids: $\boldsymbol{\sigma}^{i+1}_s = {}^n\hat{\boldsymbol{\sigma}}_s + \Delta t\ \boldsymbol{\sigma}^{\triangledown,i+1}_s$ with $\boldsymbol{\sigma}^{\triangledown,i+1}_s = \boldsymbol{c}^{\sigma J} : \boldsymbol{d}_s\left(\bar{\boldsymbol{v}}^{i+1}_s\right)$

6. Check the convergence: $\dfrac{\|\Delta\bar{\boldsymbol{v}}^{i+1}_{f,s}\|}{\|{}^n\bar{\boldsymbol{v}}_{s,f}\|} \leq e_v \quad \dfrac{\|\bar{\boldsymbol{p}}^{i+1}_f - \bar{\boldsymbol{p}}^i_f\|}{\|{}^n\bar{\boldsymbol{p}}_f\|} \leq e_p$

If condition 6 is not fulfilled, return to 1 with $i \leftarrow i+1$.

At the end of each time step, for solid elements compute

${}^{n+1}\hat{\boldsymbol{\sigma}}_s = {}^{n+1}\boldsymbol{\sigma}_s + \Delta t\boldsymbol{\Omega}_s\ ({}^{n+1}\bar{\boldsymbol{v}}_s, {}^{n+1}\boldsymbol{\sigma}_s)$

Algorithm 1: Iterative solution scheme for FSI problem solved with the V-element for solids and the VPS/F-element for fluids.

Algorithm 2 shows the procedure for solving the FSI problem using the VP-element or the VPS/S-element for the solid and the VPS/F-element for the fluid.

In Algorithms 1 and 2, e_v and e_p are prescribed error norms for the nodal velocities and the nodal pressures, respectively. In the examples solved in this work, $e_v = e_p = 10^{-4}$ has been fixed. The number of non linear iterations depends on the problem and the time step increment. For the problems solved in this publication, the average number of required iterations is around 5 for both schemes.

As explained before, the nodes at a fluid-solid interface have two different pressure degrees of freedom. As a consequence, the mass balance equations are solved separately for the fluid and the solid. In particular, the mass balance equation is solved twice at the interface nodes. All this increases the computational cost of the analysis with respect to the coupling with the V-element described in Algorithm 1. On the other hand, this scheme is more general because it allows us to solve FSI problems where incompressible solids are involved.

For each iteration i:

1. Compute the nodal velocity increments $\boldsymbol{\Delta\bar{v}}_{s,f}$:

$\boldsymbol{K}^i_{s,f}\boldsymbol{\Delta\bar{v}}_{s,f} = \boldsymbol{R}^i_{s,f}(\bar{\boldsymbol{v}}^i_{s,f}, \bar{\boldsymbol{p}}^i_{s,f})$

where for fluids: $\boldsymbol{K}^i_f = \boldsymbol{K}^m(\bar{\boldsymbol{x}}^i, \boldsymbol{c}^{\triangledown\sigma}_{NF}) + \boldsymbol{K}^g(\bar{\boldsymbol{x}}^i, \boldsymbol{\sigma}^i_f) + \boldsymbol{K}^\rho(\bar{\boldsymbol{x}}^i)$

and for solids: $\boldsymbol{K}^i_s = \boldsymbol{K}^m(\bar{\boldsymbol{x}}^i, \boldsymbol{c}^{\sigma J}) + \boldsymbol{K}^g(\bar{\boldsymbol{x}}^i, \boldsymbol{\sigma}^i_s) + \boldsymbol{K}^\rho(\bar{\boldsymbol{x}}^i)$

2. Update the nodal velocities: ${}^{n+1}\bar{\boldsymbol{v}}^{i+1}_{s,f} = {}^{n+1}\bar{\boldsymbol{v}}^i_{s,f} + \boldsymbol{\Delta\bar{v}}_{s,f}$

3. Update the nodal coordinates: ${}^{n+1}\bar{\boldsymbol{x}}^{i+1}_{s,f} = {}^{n+1}\bar{\boldsymbol{x}}^i_{s,f} + \bar{\boldsymbol{u}}_{s,f}(\boldsymbol{\Delta\bar{v}}_{s,f})$

4. Compute the fluid nodal pressures $\bar{\boldsymbol{p}}^{i+1}_f$: $\boldsymbol{H}_f\bar{\boldsymbol{p}}^{i+1}_f = \boldsymbol{F}_{pf}(\bar{\boldsymbol{v}}^{i+1}_f, \bar{\boldsymbol{p}}^i_f)$

where: $\boldsymbol{H}_f = \left(\frac{1}{\Delta t}\mathbf{M}_{1f} + \frac{1}{\Delta t^2}\mathbf{M}_{2f} + \mathbf{L}_f + \mathbf{M}_{bf}\right)$

and $\boldsymbol{F}_{pf} = \frac{\mathbf{M}_{1f}}{\Delta t}{}^n\bar{\boldsymbol{p}}_f + \frac{\mathbf{M}_{2f}}{\Delta t^2}\left({}^n\bar{\boldsymbol{p}}_f + {}^n\dot{\bar{\boldsymbol{p}}}_f\Delta t\right) + \mathbf{Q}^T\ \bar{\boldsymbol{v}}^{i+1}_f + \boldsymbol{f}_{pf}$

5. Compute the solid nodal pressures $\bar{\boldsymbol{p}}^{i+1}_s$: $\boldsymbol{H}_s\bar{\boldsymbol{p}}^{i+1}_s = \boldsymbol{F}_{ps}(\bar{\boldsymbol{v}}^{i+1}_s, \bar{\boldsymbol{p}}^i_s)$

For the VP-element: $\boldsymbol{H}_s = \frac{1}{\Delta t}\mathbf{M}_{1s}$

and $\boldsymbol{F}_{ps} = \mathbf{Q}^T\ {}^{n+1}\bar{\boldsymbol{v}}^{i+1}_s + \frac{\mathbf{M}_{1s}}{\Delta t}{}^n\bar{\boldsymbol{p}}_s$

For the VPS/S-element: $\boldsymbol{H}_s = \left(\frac{1}{\Delta t}\mathbf{M}_{1s} + \frac{1}{\Delta t^2}\mathbf{M}_{2s} + \mathbf{L}_s + \mathbf{M}_{bs}\right)$

and $\boldsymbol{F}_{ps} = \frac{\mathbf{M}_{1s}}{\Delta t}{}^n\bar{\boldsymbol{p}}_s + \frac{\mathbf{M}_{2s}}{\Delta t^2}\left({}^n\bar{\boldsymbol{p}}_s + {}^n\dot{\bar{\boldsymbol{p}}}_s\Delta t\right) + \mathbf{Q}^T\ \bar{\boldsymbol{v}}^{i+1}_s + \boldsymbol{f}_{ps}$

6. Compute the updated stress measures

for fluids: $\boldsymbol{\sigma}^{i+1}_f = 2\mu\boldsymbol{d}'_f(\bar{\boldsymbol{v}}^{i+1}_f) + p^{i+1}_f\boldsymbol{I}$

for solids: $\boldsymbol{\sigma}^{i+1}_s = {}^n\hat{\boldsymbol{\sigma}}_s + \bar{p}^{i+1}_s\boldsymbol{I} + 2\mu\Delta t\left[\mathbf{I}' : \boldsymbol{d}_s\left(\bar{\boldsymbol{v}}^{i+1}_s\right)\right]$

7. Check the convergence: $\dfrac{\|\Delta\bar{\boldsymbol{v}}^{i+1}_{f,s}\|}{\|{}^n\bar{\boldsymbol{v}}_{s,f}\|} \leq e_v \quad \dfrac{\|\bar{\boldsymbol{p}}^{i+1}_{f,s} - \bar{\boldsymbol{p}}^i_{f,s}\|}{\|{}^n\bar{\boldsymbol{p}}_{f,s}\|} \leq e_p$

If condition 7 is not fulfilled, return to 1 with $i \leftarrow i+1$.

At the end of each time step, for the solid elements

${}^{n+1}\hat{\boldsymbol{\sigma}}_s = {}^{n+1}\boldsymbol{\sigma}_s + \Delta t\boldsymbol{\Omega}_s\ ({}^{n+1}\bar{\boldsymbol{v}}_s, {}^{n+1}\boldsymbol{\sigma}_s)$

Algorithm 2: Iterative solution scheme for FSI problem solved with the VP or the VPS/S element for solids and the VPS/F-element for fluids.

8. Assembly of the global linear system and interface detection

The assembly of the global linear system is performed by looping over all the nodes of the mesh. Each node provides the contributions of the elements that share the node and each element is computed according to the specific constitutive law and the solution scheme chosen. So, when an interface node is analyzed, it is necessary to sum the contributions of both materials in the global linear system. Because the fluid and the solid pressures are two different degrees of freedom, the fluid elements assemble only the contributions for the fluid pressure, while the solid elements do that for the solid pressure.

In order to ensure the coupling, the fluid and the solid meshes must have in common the nodes along the interface. In other words, there must be a node to node conformity. This is guaranteed by exploiting the capability of the PFEM for detecting the boundaries [41]. The fluid detects the solid interface nodes in the same way it recognizes its rigid contours. In fact, the solid keeps the same discretization for all the duration of the analysis, but its boundary nodes are involved in the fluid remeshing process. This is performed via a robust algorithm [42] that combines efficiently the Alpha Shape method [14] and the Delaunay triangulation. According to this strategy, if the separation of the fluid contour from the solid domain is small enough so that that the Alpha Shape criteria are fulfilled, a fluid element connecting the fluid domain to the solid domain is generated. Otherwise the two domains keep apart from each other.

In Figure 1 a graphic representation of this technique.

9. Numerical examples

We present several examples for validating the Unified formulation. Three FSI problems are presented and other numerical results are compared to the numerical solutions. A comparison between the three solid elements (V, the VP and the VPS/S elements) derived in this work is also given for all the problems presented. In all the numerical examples, the effect of the air has not been taken into account and the VPS/F-element has been used for the fluid part of

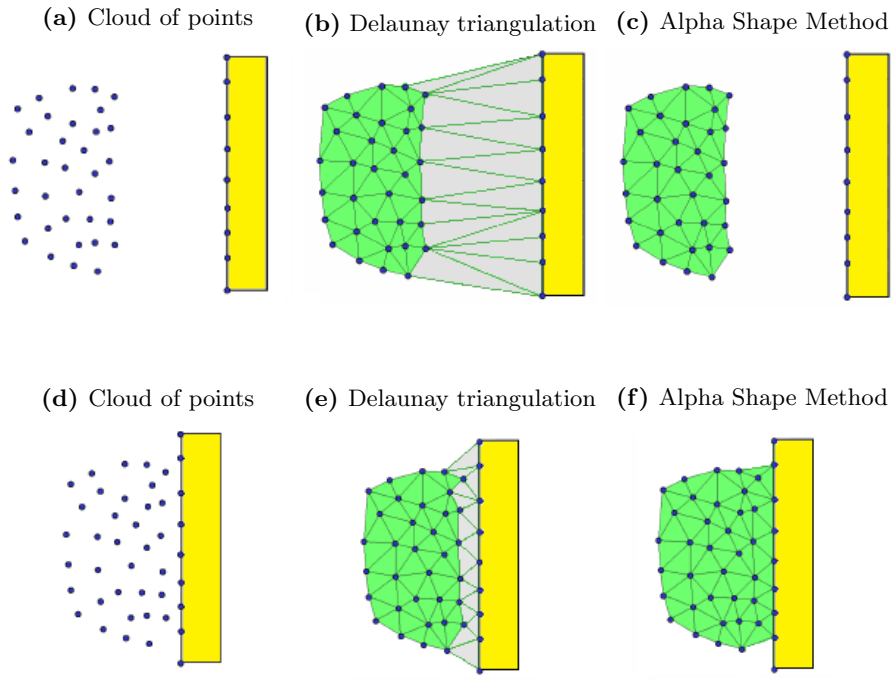

Figure 1: Detection of an interface with the PFEM [43].

the domain. The numerical examples involve large displacements of the solid structures and free surface flows. These features increase the complexity of the problems.

9.1. Falling of a cylinder in a viscous fluid

The problem is a two-dimensional (2D) abstraction of the displacement of a circular solid cylinder between two parallel walls. The cylinder moves prependicularly to its axis due to the gravity force increasing the falling velocity until an asymptotic value.

The distance from the rigid walls and the axis of the cylinder is $l = 0.02m$. The radius of the circle is $a = 0.0025m$. The geometry of the problem and the material data are given in Figure 2 and Table 2.

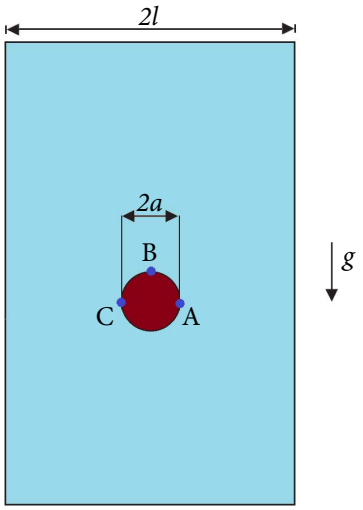

Figure 2: Falling of a cylinder in a viscous fluid. Initial geometry.

Geometric data	
l	$0.02\ m$
a	$0.0025\ m$
g	$9.81\ m/s^2$
Fluid data	
Density	$1.0{\cdot}10^3\ kg/m^3$
Viscosity	$0.1\ Pa \cdot s$
Solid data	
Density	$1.2{\cdot}10^3\ kg/m^3$
Young modulus	$10^7 GPa$
Poisson ratio	0.35, 0.4999

Table 2: Falling of a cylinder in a viscous fluid. Problem data.

The solid cylinder has been modeled as a quasi-rigid body with an hypoelastic model and a high value for the Young modulus. The VP formulation has been used for the solid.

This numerical example was already studied in other publications [44, 45, 46]. For the fluid viscosity $0.1 Pa \cdot s$ and slip conditions on the walls, the cited works give the velocity of fall of the cylinder reaching an asymptotic value of around $U_{max} = 0.037 m/s$.

In this work, the problem has been solved for both stick and slip conditions on the vertical walls of the container, while the fluid-solid interface has been modeled with no-slip conditions, in all the studied problems.

In Figure 3 the velocity field obtained considering slip boundary conditions is given for three time instants.

In Figure 4, the results for the stick case for the same time instants of Figure 3 are given.

The resulting pressure field for the slip and stick cases is illustrated in Figure 5.

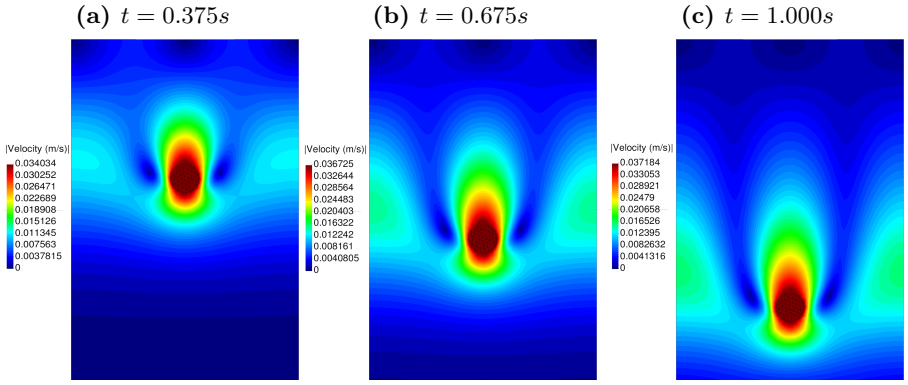

Figure 3: Falling of a cylinder in a viscous fluid. 2D simulation of the slip case. Snapshots of the cylinder motion with velocity contours at different instants.

The pictures show that the perturbation over the fluid pressure field caused by the motion of the cylinder is almost imperceptible and there are not significant differences between the slip and stick cases.

In the graph of Figure 6 the time evolution of the vertical velocity of the cylinder obtained with the finest mesh of 3-noded triangles (average size=$0.0004m$) is given for both the slip and stick cases.

The terminal velocities of the cylinder obtained for the slip and the stick cases are $0.0377m/s$ (giving a difference of around 1,8% with respect to the reference works) and $0.0336m/s$, respectively.

For this example the transmission conditions between the solid and the fluid domain have been monitored. The curves of Figure 7 represent the time evolution of the Neumann conditions in the X-direction (horizontal) at the points A, B, C located at the boundary of the cylinder and depicted in Figure 2. Specifically, the value plotted in the curves is the mean value of the X-component of vector $\boldsymbol{\sigma n}$ $(\sigma_{xx} n_x + \tau_{xy} n_y)$ computed for the fluid and the solid elements at the points A, B, C of Figure 2. The graph shows that the transmission condition is guaranteed during all the analysis thanks to the monolithic solution of the FSI problem.

The problem has been solved also for a quasi-incompressible solid using the

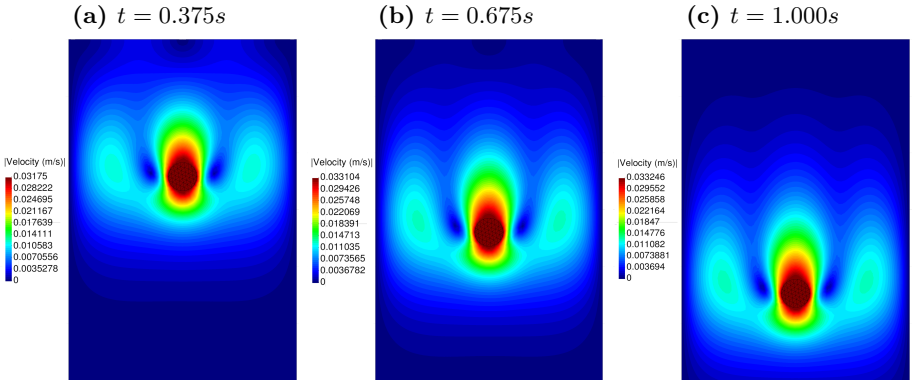

Figure 4: Falling of a cylinder in a viscous fluid. 2D simulation of the stick case. Snapshots of the cylinder motion with velocity contours at different instants.

VPS/S-element. For this analysis, a Poisson ratio of 0.4999 and the same Young modulus of the previous case have been considered. The simulation has been run considering stick conditions on the walls and using a mean mesh size of $0.007m$, as for the problem plotted in Figure 4. In Figure 8 the velocity and the pressure fields for the solid and the fluid computed at $t = 1s$ are given.

In the graph of Figure 9 the time evolution of the vertical velocity obtained with the VPS/S-element for $\nu = 0.4999$ is compared to the solution obtained with the VP-element for $\nu = 0.35$ and the same average mesh size and boundary conditions.

Figure 9 shows that the solutions are almost the same and the vicinity to the incompressible limit does not affect the quality of the results.

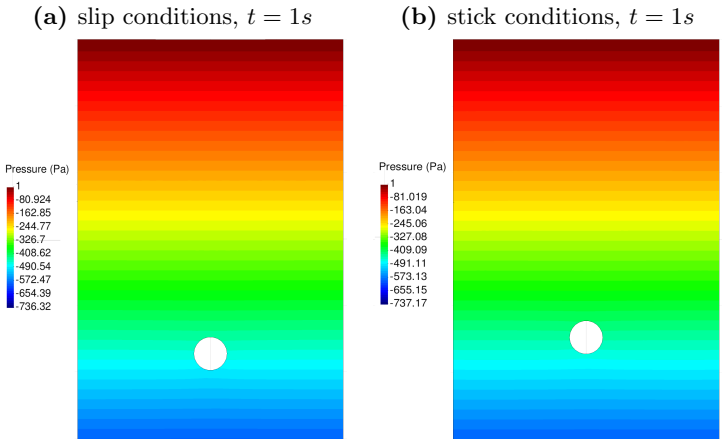

Figure 5: Falling of a cylinder in a viscous fluid. Pressure field obtained for the slip and stick cases.

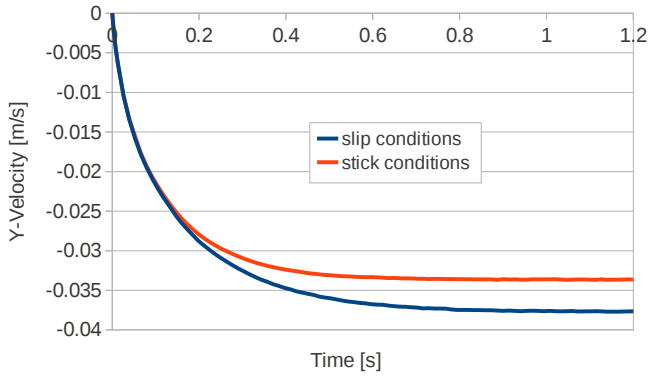

Figure 6: Falling of a cylinder in a viscous fluid. Time evolution of the vertical velocity of the cylinder. Results for the slip and stick cases.

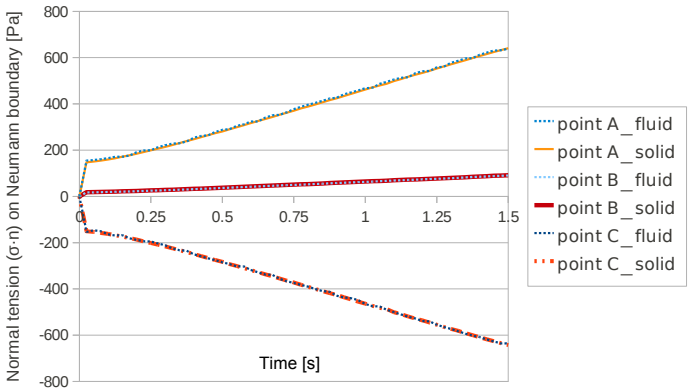

Figure 7: Falling of a cylinder in a viscous fluid. Time evolution of the X-component of $\sigma_{xx}n_x + \sigma_{xy}n_y$ computed at the points A, B, C of Figure 2.

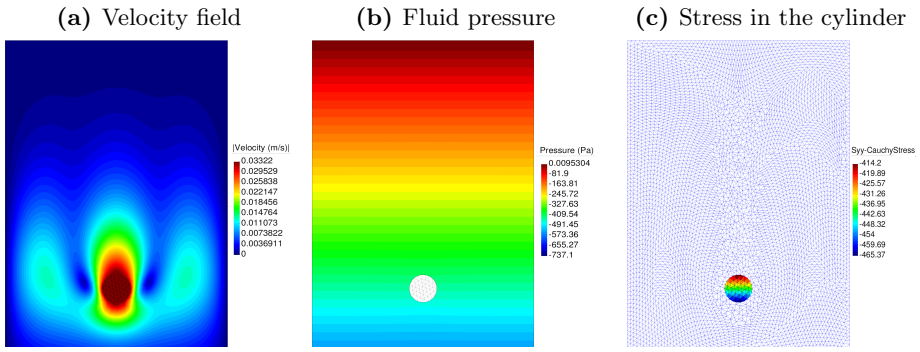

Figure 8: Falling of a cylinder in a viscous fluid. Quasi-incompressible solid ($\nu = 0.4999$). Velocity and the pressure fields and solid Cauchy stress (YY-component) at $t = 1s$ for stick conditions on the walls and a mean mesh size of $0.007m$.

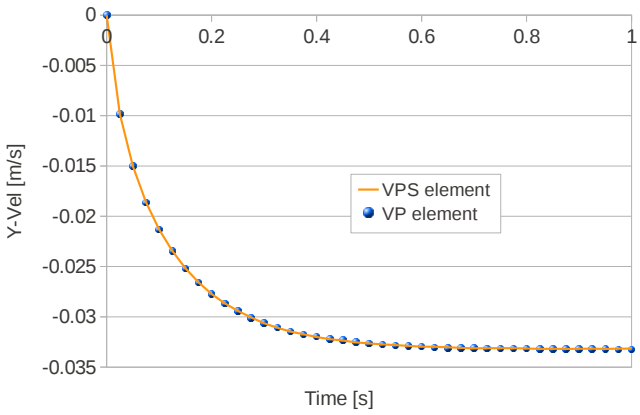

Figure 9: Falling of a cylinder in a viscous fluid. Solutions obtained with two different elements for the solid: the VP-element ($\nu = 0.35$) and the VPS/S-element ($\nu = 0.4999$).

9.2. Filling of an elastic container with a viscous fluid

This example has been inspired from a similar problem presented in [47]. A volume of a viscous fluid drops from a rigid container over a thin and highly deformable elastic membrane. The impact of the fluid mass causes an initial huge stretching of the structure and its subsequent oscillations. Two horizontal rigid walls are placed at the top of the elastic container in order to avoid the leackage of the fluid. The problem was solved in 2D for two different values of the fluid viscosity, namely 50 and 100 $Pa \cdot s$. For the structure, both the V and VP elements presented in this work have been used. The purpose was to compare the formulations and to show that both solid elements can be used for the modeling of standard elastic solids in FSI problems. The initial geometry of the problem is given in Figure 3 and the material data are given in Table 3.

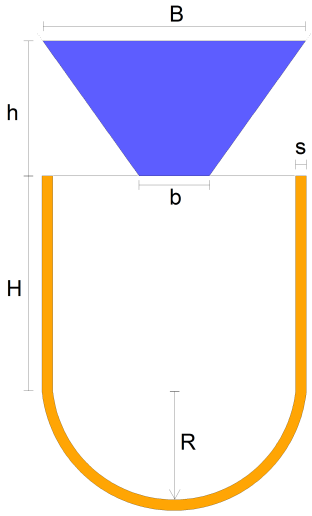

Figure 10: Filling of an elastic container with a viscous fluid. Initial geometry.

Geometry data	
h	2.5 m
H	3.75 m
R	2.25 m
b	1.3 m
B	4.8714 m
s	0.2 m
Fluid data	
Viscosity	50, 100 $Pa \cdot s$
Density	1000 kg/m^3
Solid data	
Young modulus	2.1 $10^7 GPa$
Poisson ratio	0.3
Density	20 kg/m^3

Table 3: Filling of an elastic container with a viscous fluid. Problem data.

The solid and the fluid domains have been discretized with a mesh composed by 9363 3-noded triangles.

In the graph of Figure 11 the results for the less viscous case (μ=50 Pa·s) obtained using the V and the VP elements for the solid are given. The comparison is performed for the vertical displacement of the lowest point of the elastic structure.

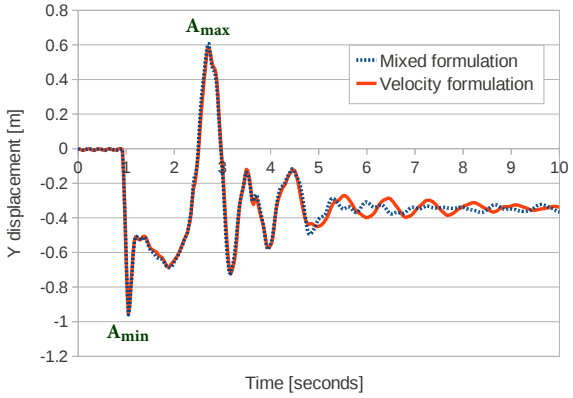

Figure 11: Filling of an elastic container with a viscous fluid ($\mu = 50Pa \cdot s$). Vertical displacement of the bottom of the container obtained using the V and the VP elements for the solid domain.

The curves are almost coincident and only after $4.5s$ of simulation some slight differences appear.

In Table 4 the maximum and the minimum vertical displacements of the elastic structure obtained with the V and the VP elements are shown. A_{min} and A_{max} refer to the minimum and maximum points of the curves of Figure 11. The numerical results obtained with the two solid elements are very close.

Point	V-element		VP-element	
	time instant	vertical disp.	time instant	vertical disp.
A_{min}	1.045 s	-0.951 m	1.045 s	-0.961 m
A_{max}	2.695 s	0.586 m	2.695 s	0.606 m

Table 4: Filling of an elastic container with a viscous fluid ($\mu = 50Pa \cdot s$). Maximum and minimum vertical displacements for the V and the VP elements.

For the same problem, some representative snapshots are collected in Figure 12. Over the solid domain the pressure contours are depicted and over the fluid one the mesh is plotted. The numerical results correspond to the simulation using the VP-element for the solid.

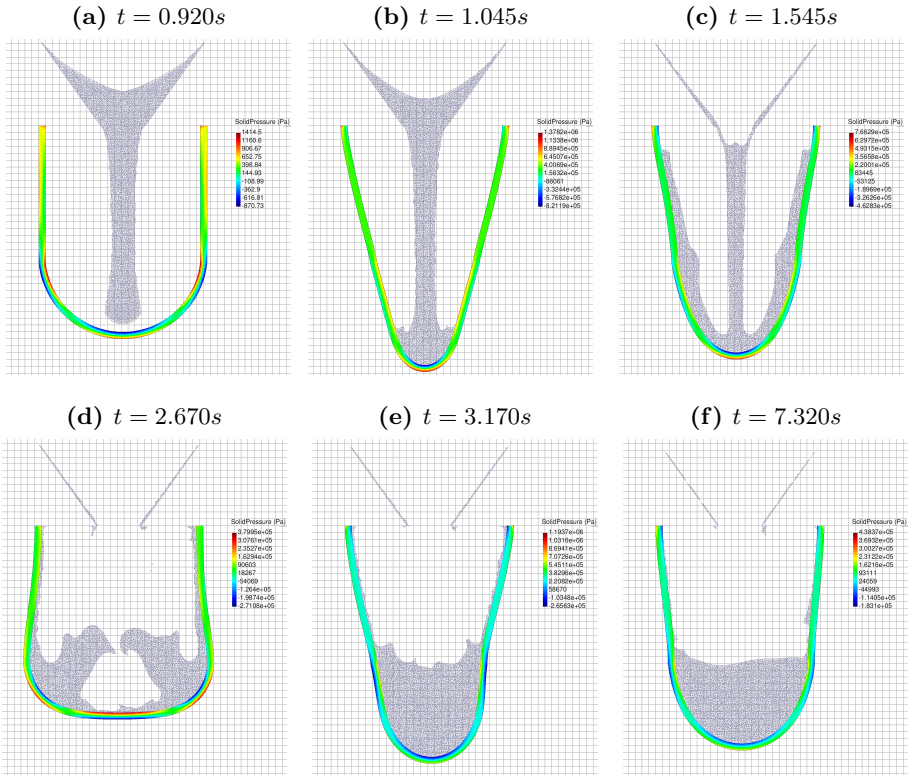

Figure 12: Filling of an elastic container with a viscous fluid ($\mu = 50Pa{\cdot}s$). Snapshots of the numerical simulation at different instants. Pressure contours are depicted over the solid domain.

In Figure 13 snapshots of the numerical simulation for the most viscous case (μ=100 Pa·s) are given for the same time instants of Figure 12. The numerical results correspond again to the solution obtained using the VP-element for the solid domain.

The results obtained with the V and VP elements for the solid are compared

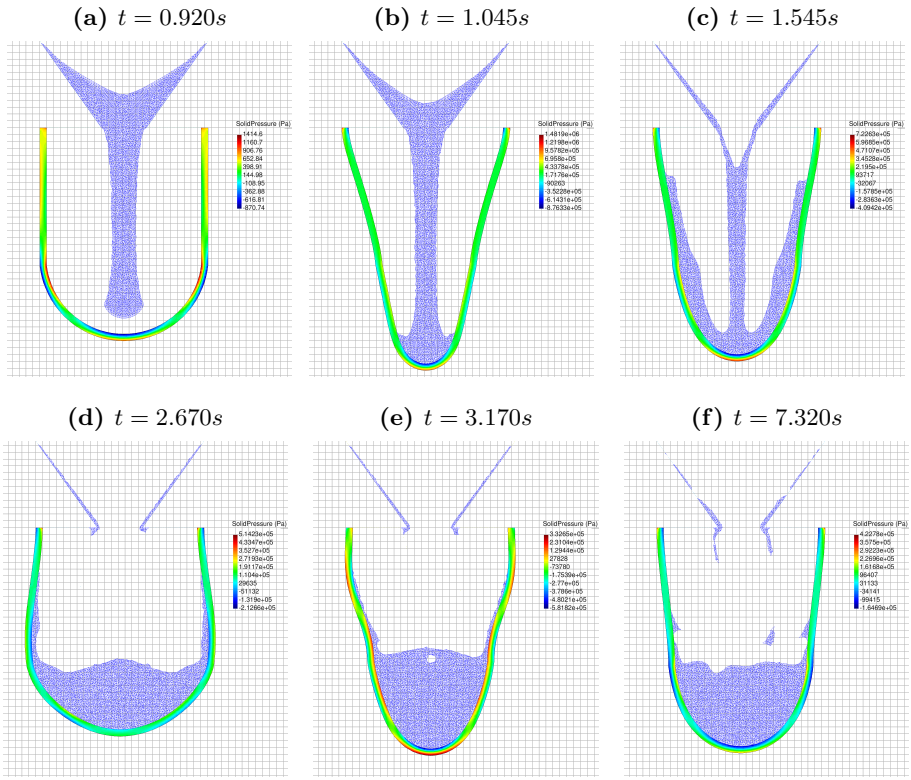

Figure 13: Filling of an elastic container with a viscous fluid ($\mu = 100Pa \cdot s$). Snapshots at different instants of the 2D simulation. Pressure contours depicted over the solid domain.

for the most viscous case analyzing the time evolution of the vertical displacement at the bottom of the container. In Figure 14 the solutions obtained using both elements are plotted.

Once again, the differences between the results of the two formulations for the solid are very small. This is a further evidence of the validity and flexibility of the Unified formulation, that allows us to choose for the solid either a velocity or a mixed formulation.

The maximum and the minimum vertical displacements of the structure obtained by the V and the VP elements are collected in Table 5. B_{min} and

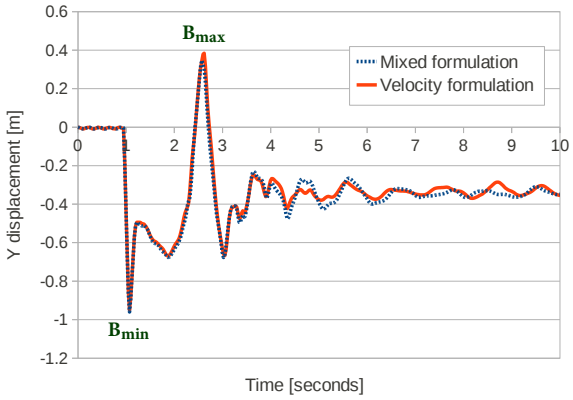

Figure 14: Filling of an elastic container with a viscous fluid ($\mu = 100Pa \cdot s$). Vertical displacement of the bottom of the elastic container obtained using the V and the VP elements for the solid domain.

B_{max} correspond to the points marked in the graph of Figure 14.

Point	V-element		VP-element	
	time instant	vertical disp.	time instant	vertical disp.
B_{min}	1.070 s	-0.950 m	1.070 s	-0.960 m
B_{max}	2.620 s	0.384 m	2.570 s	0.347 m

Table 5: Filling of an elastic container with a viscous fluid ($\mu = 100Pa \cdot s$). Maximum and minimum vertical displacements for the V and the VP elements.

Comparing the results of Tables 4 and 5, one may note that the lowest position of the structure is almost the same for both problems, although in the most viscous case it is reached slightly later. For the maximum upward displacement, the differences between the two problems are bigger. In fact, the maximum upward displacement of the container is significally larger for the less viscous fluid and the highest position is reached later. This is so because the less viscous fluid splashes more and moves away from the bottom of the elastic container, reducing the weight acting on the container walls.

9.3. Collapse of a water column on a deformable membrane

The problem illustrated in Figure 15 was introduced by Walhorn *et al.* [48].

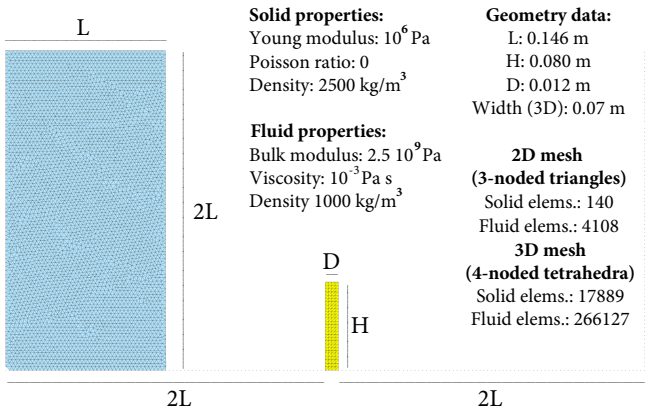

Figure 15: Collapse of a water column on a deformable membrane. Initial geometry and problem data.

The water column collapses by instantaneously removing the vertical wall. This originates the flow of water within the tank, the formation of a jet after the water stream hits the ground, and the subsequent sloshing of the fluid as it impacts a highly deformable elastic membrane. The membrane bends and starts oscillating under the effect of its inertial forces and the impact with the water stream.

In Figure 16 some representative snapshots of the 2D simulation are given. The VP-element for the solid was used for the analysis.

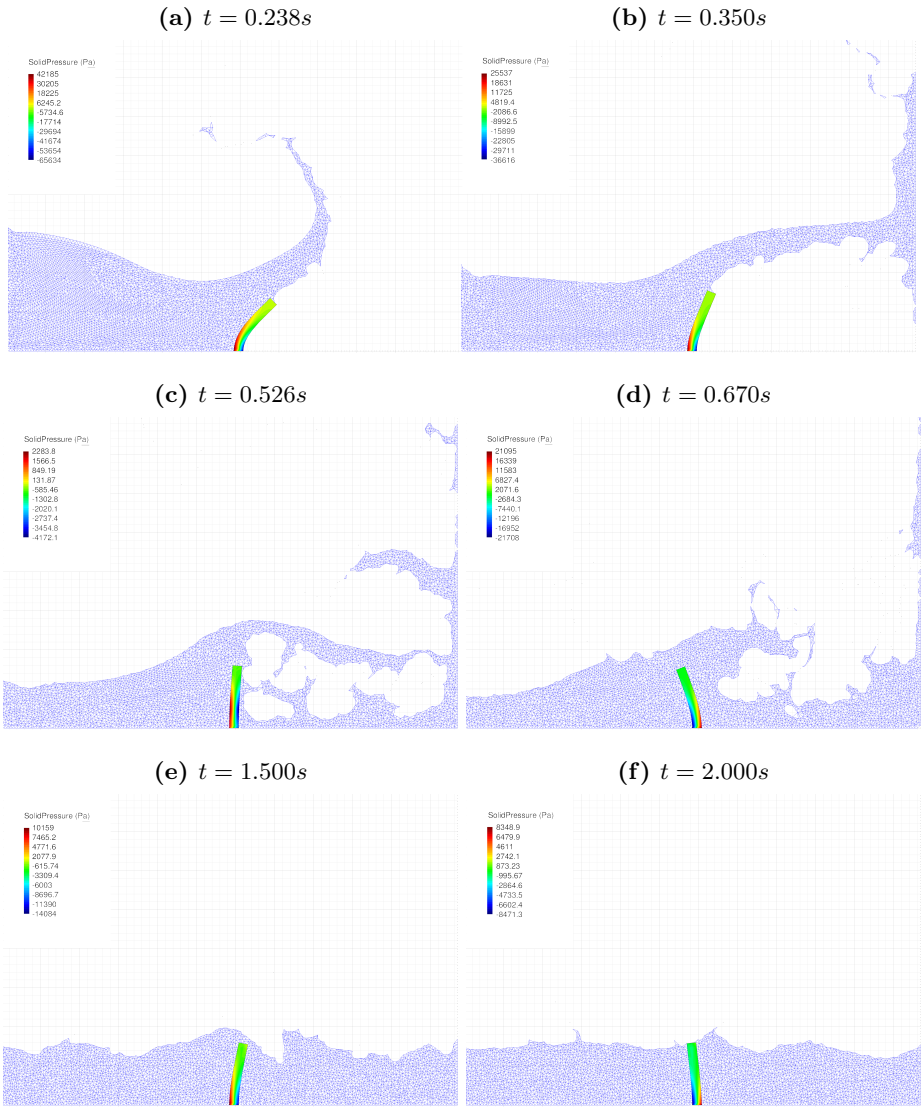

Figure 16: Collapse of a water column on a deformable membrane. Snapshots of the 2D simulation at different instants. The VP-element is used for the solid.

The results obtained with the present formulation using the V-element and the VP-element for the solid have been compared to the ones computed in [49, 1, 43]. In the graph of Figure 17 the time evolution of the horizontal deflection of the left top corner is illustrated.

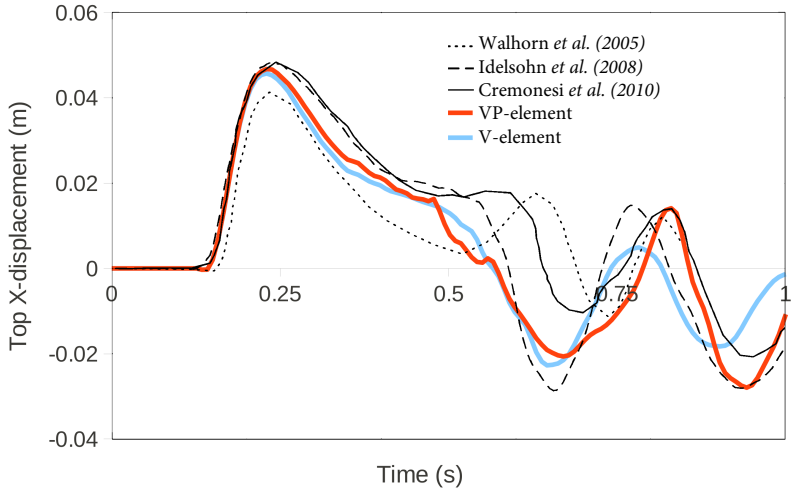

Figure 17: Collapse of a water column on a deformable membrane. Horizontal deflection of the left top corner on time. Numerical results obtained with the V and VP elements for the solid. Comparison with numerical results obtained in [48, 1, 43].

The diagram shows that for the first part of the analysis the proposed formulation agrees well with the results reported in the literature. After around $0.5s$ of simulation, the numerical results of each formulation start to disagree. However, for all cases the membrane oscillates two times around its vertical position before the time instant $t = 1s$.

The first part of the simulation is easier to analyze than the second one because the phenomena to model are less aleatory and the fluid splashes do not affect the results, as it occurs after $0.5s$. Furthermore, the differences between the numerical simulations accumulate throughout the analysis. In other words, a slight difference in the first part of the simulation may produce a huge variation of the results for the rest of the analysis. In fact, the inital deformation of the elastic structure affects highly the results: a smaller bending of the membrane

induces an impact of the water stream at an higher height of the containing wall and with a bigger tangential component of the impact velocity. Consequently, the fluid stream impacts with the right side of the elastic membrane later and with reduced inertial forces.

The same example has been solved also in 3D. A width of $0.07m$ for the prismatic tank been considered for the z-direction. In order to maintain the plane strain state of the 2D problem, in the 3D analysis the nodal displacements of the elastic membrane in the z-direction have been constrained. The mesh data of the 3D problem are given in Figure 15. In this analysis the V-element has been used for the solid.

In Figure 18 the numerical results of the 3D simulation are given.

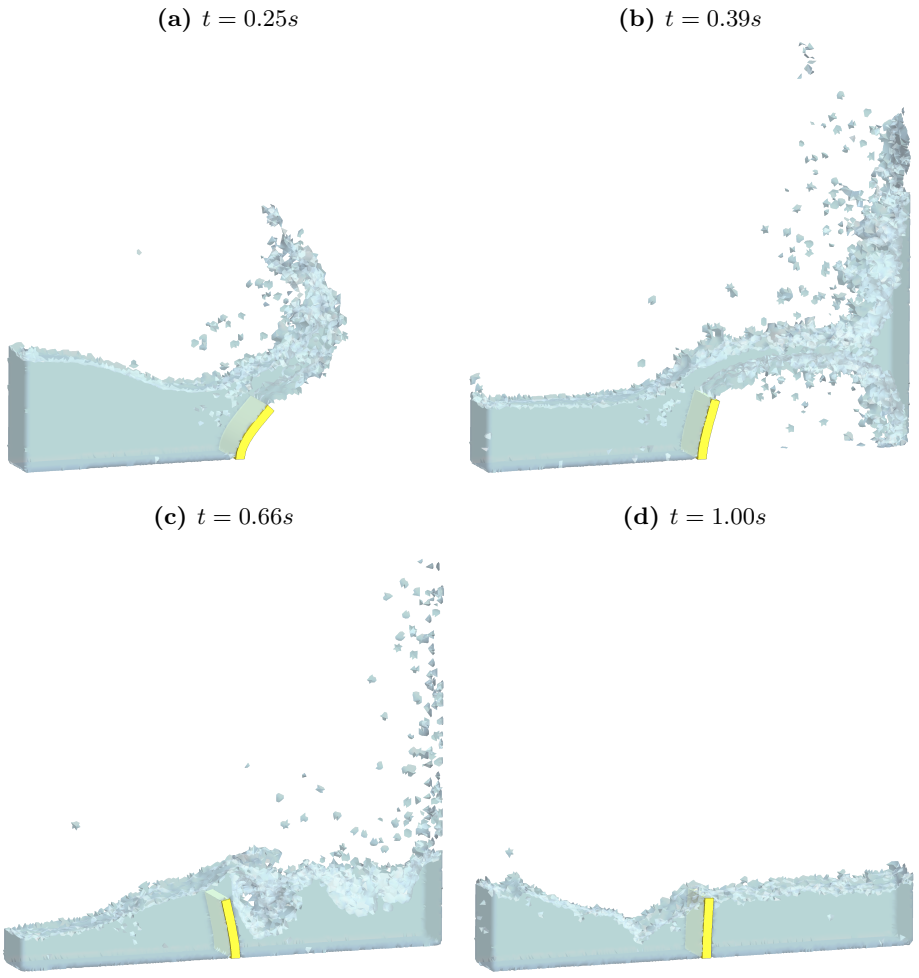

Figure 18: Collapse of a water column on a deformable membrane. Snapshots of the 3D simulation of different instants. The V-element is used for the solid.

For the same time instants of Figure 18, in Figure 19 the velocity contours are plotted over the cutting plane built at $z = 0.035m$.

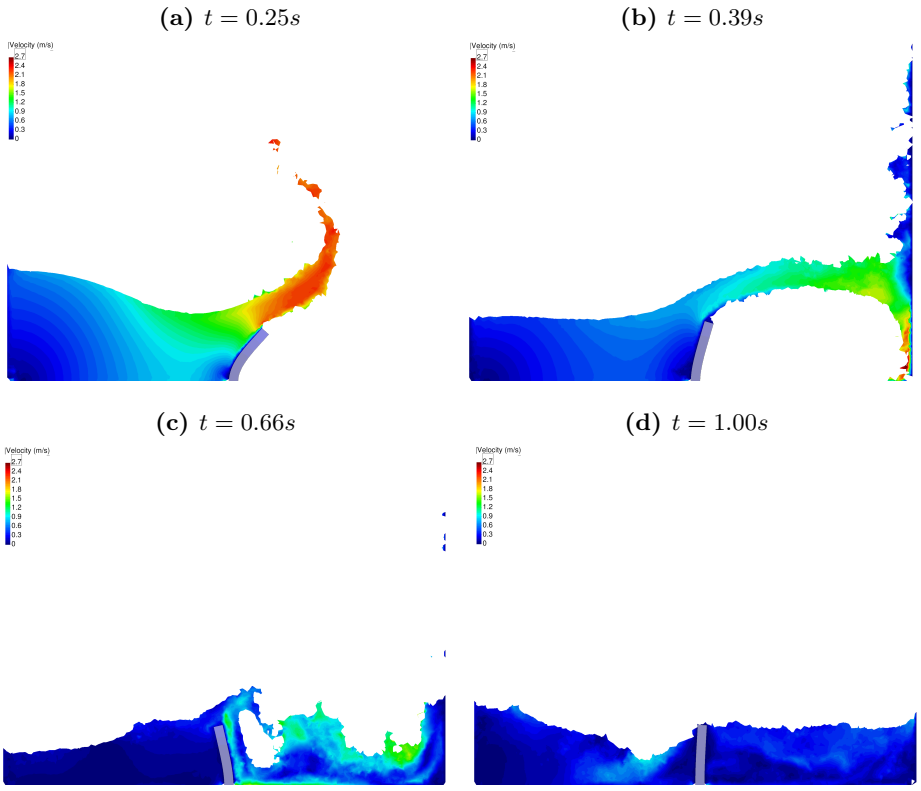

Figure 19: Collapse of a water column on a deformable membrane. Velocity contours plotted over the plane located at $z = 0.035m$ of the 3D domain. The V-element is used for the solid.

No numerical or experimental results have been found in the literature for the described 3D abstraction of the 2D benchmark problem presented in [48]. For this reason, 3D results have been compared only to the analogous 2D problem solved with the proposed formulation. Figure 20 shows the time evolution of the 2D and 3D results for the horizontal deflection of the left top corner obtained with the V-element for the solid.

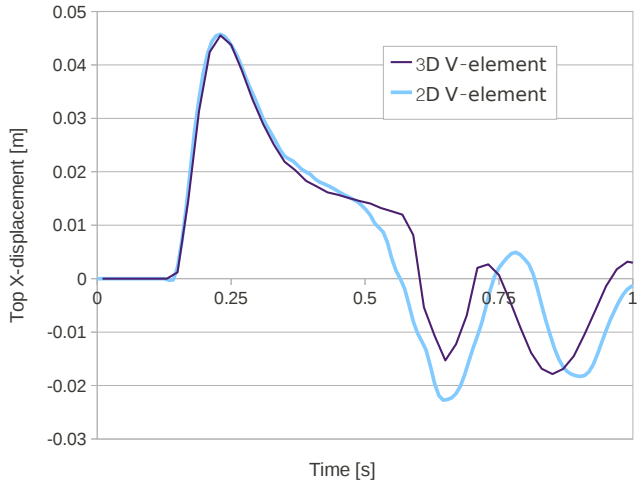

Figure 20: Collapse of a water column on a deformable membrane. Horizontal deflection of the left top corner on time. Comparison between 2D and 3D analyses for the V-element.

Figure 20 shows that the 3D results agree well with those of the 2D analysis for the first part of the simulation. After around $0.5s$ the two graphs start to diverge. In particular, in the 3D analysis the water stream hits the right side of the membrane later and with a reduced impact force with respect to the 2D problem. This is due to the 3D effects. In fact, if the plane strain hypotesis is not satisfied exactly, the fluid can expand also in the z-direction reducing its impact velocity against the structure. Clearly, the mesh refinement can reduce these effects and, consequently, also the differences between the 3D and the 2D simulations.

10. Concluding remarks

In this work, a Unified formulation for fluid and solid mechanics and FSI problems has been presented.

For incompressible materials the mixed velocity-pressure formulation is stabilized using the FIC-FEM procedure derived in [9] for Newtonian fluids and applied in this work also for quasi-incompressible hypoelastic solids.

For the solid parts of the domain, three different hypoelastic elements have been presented, namely the V, the VP and the VPS/S elements respectively based on a velocity, mixed velocity-pressure and mixed velocity-pressure stabilized formulation.

The Unified formulation, through an efficient combination of the PFEM for the fluid, and the FEM for the solid, allows us to solve FSI problems in a monolithic way ensuring automatically a strong coupling. Furthermore, the risk of ill-conditioning in the global linear system of algebraic equations is reduced using the same unknown variables for the fluid and the solid and solving the global problem through a partitioned scheme.

The efficiency of the method has been tested by solving FSI benchmark problems involving free surface viscous flows and large displacements for the structure. Good agreement between the results obtained with the present formulation and published results has been found in all cases for all the solid elements derived in this work.

Acknowledgements

This work was partially supported by the SAFECON Advanced Grant project and the FLOODSAFE Proof of Concept project of the European Research Council.

References

[1] S. R. Idelsohn, J. Marti, A. Limache, E. Oñate, Unified lagrangian formulation for elastic solids and incompressible fluids: Applications to fluid-structure interaction problems via the pfem, Computer Methods In Applied Mechanics And Engineering 197 (2008) 1762–1776.

[2] F. Brezzi, On the existence, uniqueness and approximation of saddle-point problems arising from lagrange multipliers, Revue française d'automatique, informatique, recherche opérationnelle. Série rouge. Analyse numérique 8(R-2) (1974) 129–151.

[3] F. Felippa, E. Oñate, Nodally exact ritz discretizations of 1d diffusion-absorption and helmholtz equations by variational fic and modified equation methods, Computational Mechanics 39 (2007) 91–111.

[4] E. Oñate, Derivation of stabilized equations for advective-diffusive transport and fluid flow problems, Computer methods in applied mechanics and engineering 151 (1998) 233–267.

[5] E. Oñate, A. Valls, J. García, Fic/fem formulation with matrix stabilizing terms for incompressible flows at low and high reynold's numbers., Computational mechanics 38 (4-5) (2006) 440–455.

[6] E. Oñate, J. García, S. R. Idelsohn, F. D. Pin, Fic formulations for finite element analysis of incompressible flows. eulerian, ale and lagrangian approaches., Computer methods in applied mechanics and engineering 195 (23-24) (2006) 3001–3037.

[7] E. Oñate, P. Nadukandi, S. R. Idelsohn, J. García, C. Felippa, A family of residual-based stabilized finite element methods for stokes flows, International Journal for Numerical Methods in Fluids 65(1-3) (2011) 106–134.

[8] E. Oñate, S. R. Idelsohn, C. Felippa, Consistent pressure laplacian stabilization for incompressible continua via higher-order finite calculus, In-

ternational Journal of Numerical Methods in Engineering 87(1:5) (2011) 171–195.

[9] E. Oñate, A. Franci, J. M. Carbonell, Lagrangian formulation for finite element analysis of quasi-incompressible fluids with reduced mass losses, International Journal for Numerical Methods in Fluids 74 (10) (2014) 699–731.

[10] W. Prager, Introduction to Mechanics of Continua, Ginn and Company, Boston, 1961.

[11] A. Franci, Doctoral thesis: Unified Lagrangian formulation for fluid and solid mechanics, fluid-structure interaction and coupled thermal problems using the PFEM, 2015.

[12] O. C. Zienkiewicz, R. L. Taylor, The Finite Element Method. Its Basis and Fundamentals. (6th Ed.), Elsevier Butterworth-Heinemann, Oxford, 2005.

[13] S. R. Idelsohn, E. Oñate, F. D. Pin, The particle finite element method: a powerful tool to solve incompressible flows with free-surfaces and breaking waves, International Journal for Numerical Methods in Engineering 61 (2004) 964–989.

[14] H. Edelsbrunner, E. Mucke, Three dimensional alpha shapes, ACM Trans Graphics 13 (1999) 43–72.

[15] A. Larese, R. Rossi, E. Oñate, S. R. Idelsohn, Validation of the particle finite element method (pfem) for simulation of free surface flows, International Journal for Computer-Aided Engineering and Software 25 (2008) 385–425.

[16] M. Cremonesi, L. Ferrara, A. Frangi, U. Perego, A lagrangian finite element approach for the simulation of water-waves induced by landslides, Computer and Structures 89 (2011) 1086–1093.

[17] B. Tang, J. F. Li, T. S. Wang, Some improvements on free surface simulation by the particle finite element method, International Journal for Numerical Methods in Fluids 60 (9) (2009) 1032–1054.

[18] R. Aubry, S. R. Idelsohn, E. Oñate, Particle finite element method in fluid-mechanics including thermal convection-diffusion, Computers and Structures 83 (2005) 1459–1475.

[19] E. Oñate, R. Rossi, S. R. Idelsohn, K. Butler, Melting and spread of polymers in fire with the particle finite element method., International Journal of Numerical Methods in Engineering 81 (8) (2010) 1046–1072.

[20] E. Oñate, A. Franci, J. M. Carbonell, A particle finite element method (pfem) for coupled thermal analysis of quasi and fully incompressible flows and fluid-structure interaction problems, Numerical Simulations of Coupled Problems in Engineering. S. R. Idelsohn (Ed.) 33 (2014) 129–156.

[21] S. R. Idelsohn, J. Marti, P. Becker, E. Oñate, Analysis of multifluid flows with large time steps using the particle finite element method, International Journal for Numerical Methods in Engineering 75 (9) (2014) 621–644.

[22] T. S. Dang, G. Meschke, An ale-pfem method for the numerical simuation of two-phase mixture flow, Computer Methods in Applied Mechanics and Engineering 278 (2014) 599–620.

[23] X. Zhang, K. Krabbenhoft, D. Sheng, Particle finite element analysis of the granular column collapse problem, Granular Matter 16 (2014) 609–619.

[24] E. Oñate, S. R. Idelsohn, M. A. Celigueta, R. Rossi, Advances in the particle finite element method for the analysis of fluid–multibody interaction and bed erosion in free surface flows, Computer methods in applied mechanics and engineering 197 (19-20) (2008) 1777–1800.

[25] E. Oñate, M. A. Celigueta, S. R. Idelsohn, F. Salazar, B. Suarez, Possibilities of the particle finite element method for fluid–soil–structure interaction problems, Computation mechanics 48 (2011) 307–318.

[26] M. Zhu, M. H. Scott, Modeling fluid-structure interaction by the particle finite element method in opensees, Computers and Structures 132 (2014) 12–21.

[27] J. M. Carbonell, E. Oñate, B. Suarez, Modeling of ground excavation with the particle finite-element method, Journal of Engineering Mechanics 136 (2010) 455–463.

[28] E. Oñate, A. Franci, J. M. Carbonell, A particle finite element method for analysis of industrial forming processes, Computational Mechanics 54 (2014) 85–107.

[29] J. M. Carbonell, E. Oñate, B. Suarez, Modelling of tunnelling processes and cutting tool wear with the particle finite element method (pfem), Computational Mechanics 52 (3) (2013) 607–629.

[30] E. Oñate, J. M. Carbonell, Updated lagrangian finite element formulation for quasi and fully incompressible fluids, Computational Mechanics 54 (6).

[31] P. Becker, S. R. Idelsohn, E. Oñate, A unified monolithic approach for multi-fluid flows and fluid–structure interaction using the particle finite element method with fixed mesh, Computational Mechanics 61 (2015) 1–14.

[32] C. Truesdell, Hypo-elasticity, Journal of Rational Mechanics and Analysis 4,1.

[33] J. Nagtegaal, J. D. Jong, Some computational aspects of elastic-plastic large strain analysis, Numerical Methods in Engineering 17 (1) (1981) 15–41.

[34] A. Green, P. Naghdi, A general theory of an elastic-plastic continuum, Archive for Rational Mechanics and Analysis 18 (1965) 251–281.

[35] G. Johnson, D. Bammann, A discussion of the stress rate in finite deformation problems, International Journal of Solids and Structures 20 (1984) 725–737.

[36] T. Belytschko, W. K. Liu, B. Moran, K. I. Elkhodadry, Nonlinear Finite Elements For Continua And Structures. Second Edition., John Wiley & Sons, New York, 2014.

[37] P. Ryzhakov, E. Oñate, S. R. Idelsohn, Improving mass conservation in simulation of incompressible flows, International Journal of Numerical Methods in Engineering 90 (2012) 1435–1451.

[38] P. Ryzhakov, R. Rossi, S. R. Idelsohn, E. Oñate, A monolithic lagrangian approach for fluid-structure interaction problems, Computational Mechanics 46 (2010) 883–899.

[39] P. Ryzhakov, J. Cotela, R. Rossi, E. Oñate, A two-step monolithic method for the efficient simulation of incompressible flows, International Journal for Numerical Methods in Fluids 74 (12) (2014) 919–934.

[40] A. Franci, E. Oñate, J. M. Carbonell, On the effect of the bulk tangent matrix in partitioned solution schemes for nearly incompressible fluids, International Journal for Numerical Methods in Engineering DOI: 10.1002/nme.4839.

[41] E. Oñate, S. R. Idelsohn, F. D. Pin, R. Aubry, The particle finite element method. an overview, International Journal for Computational Methods 1 (2004) 267–307.

[42] S. R. Idelsohn, N. Calvo, E. Oñate, Polyhedrization of an arbitrary point set, Computer Methods in Applied Mechanics and Engineering 92 (22–24) (2003) 2649–2668.

[43] M. Cremonesi, Doctoral thesis: A Lagrangian Finite Element Method for the Interaction Between Flexible Structures and Free Surfaces Fluid Flows, 2010.

[44] A. J. Gil, A. Arranz, J. Bonet, O. Hassan, The immersed structural potential method for haemodynamic applications, Journal of Computational Physics 229 (2010) 8613–8641.

[45] C. Hesch, A. J. Gil, A. Arranz, J. Bonet, On continuum immersed strategies for fluid–structure interaction, Computer Methods in Applied Mechanics and Engineering 247 (2012) 51–64.

[46] X. Wang, W. K. Liu, Extended immersed boundary method using fem and rkpm, Computer Methods in Applied Mechanics and Engineering 193 (2004) 1305–1321.

[47] M. Cremonesi, A. Frangi, U. Perego, A lagrangian finite element approach for the analysis of fluid–structure interaction problems, International Journal of Numerical Methods in Engineering 84 (2010) 610–630.

[48] E. Walhorn, A. Kolke, B. Hubner, D. Dinkler, Fluid-structure coupling within a monolithic model involving free surface flows, Computer & Structures Methods in Applied Mechanics and Engineering 83 (25-26) (2005) 2100–2111.

[49] B. Hubner, E. Walhorn, D. Dinkler, A monolithic approach to fluid-structure interaction using space-time finite elements, Computer Methods in Applied Mechanics and Engineering 193 (2004) 2087–2104.